Entanglement spectra of engineered NMR spin Hamiltonians

A Senior Honors Thesis

Submitted to the faculty

in partial fulfillment of the requirements for the

Degree of Bachelor of Arts in

Physics

by

Kent Ueno

DARTMOUTH COLLEGE

Hanover, NH

June 2018

Entanglement spectra of engineered NMR spin Hamiltonians

A Senior Honors Thesis

Submitted to the faculty

in partial fulfillment of the requirements for the

Degree of Bachelor of Arts in

Physics

by

Kent Ueno

DARTMOUTH COLLEGE

Hanover, NH

June 2018

Chandrasekhar Ramanathan, Advisor

Lorenza Viola

James Whitfield

Abstract

Understanding how information spreads in a many-body quantum system is important, both from a fundamental physics perspective and for the development of quantum computers. One popular method is to look at the spread of entanglement, which offers insight into how information spreads. Recently two metrics, the Eigenstate Entanglement Spectrum (EES) and Entanglement Spectrum Statistics (ESS) have gained attention as theoretical metrics of entanglement for their ability to differentiate between localized and thermalized phases in some lattice spin models. EES probes entanglement of eigenstates of the Hamiltonian, while ESS examines how entangled a random product state becomes over time. Here we use the two metrics to study the properties of a class of experimentally accessible 1D nearest-neighbor coupled spin Hamiltonians that can be implemented in solid-state NMR experiments. We show that this model does indeed display a rich dynamical behavior, exhibiting features associated with integrability, thermalization, and many-body localization. In this study we identify several regimes of interest and analyze them using both metrics. Since this system can be reproduced with a model NMR system, these findings can guide the design of NMR experiments to probe these dynamical transitions.

Acknowledgements

First and foremost, I would like to thank Professor Chandrasekhar Ramanathan for all his guidance and patience. The first project I worked on in his lab gave me valuable experience with an experimental project. After some time, I decided to try theoretical work, perhaps to his dismay - but thanks to his knowledgeable aid and kindness in allowing me to pursue my interests, I was able to delve into a field that I find deeply engaging. Though he likes to poke fun at my rather embarrassing blunders, he has been an incredible advisor to have.

I would also like to thank friends and family that have supported my studies and this project in particular. I am especially grateful to my parents and grandparents who, despite limited exposure to physics, have always fully backed me in the pursuits of my interests.

Contents

Chapter 1

Introduction

This thesis explores two metrics of entanglement, the Eigenstate Entanglement Spectrum and Entanglement Spectrum Statistics, in order to characterize thermalization and localization in an experimentally accessible 1D, nearest-neighbor coupled spin-1/2 chain. We are motivated by the difficulty of exploring dynamics of large quantum many-body systems and understanding how to relate many-body dynamics to quantum information processing.

1.1 Quantum Simulation

Despite the immense success of quantum mechanics in explaining various phenomena at the atomic level, there is much to be learned about large quantum systems. Large many-body quantum systems are notoriously difficult to explore experimentally and are often impossible to simulate computation-

ally over reasonable timescales. An attractive solution to this problem is to use *quantum simulation* - the use of one controlled quantum system to explore the behavior of another less accessible quantum system. Quantum computers were proposed for quantum simulation in the early 1980s because, in principle, a large quantum system could be numerically explored using a similar number of quantum bits (qubits). In order to build such a device, however, we must first understand how to represent, store, transmit, and process quantum information in qubits.

Quantum computers can store information in qubits, which are two-state quantum systems such as spin-1/2 nuclei. We can represent a qubit as a vector in a 2×2 complex vector space where no particular basis is specified. As a concrete example, consider a basis such that the "up" state aligns with the the z axis and "down" antialigns. The qubit can be in an "up" state $|0\rangle$, a "down" state $|1\rangle$, or a superposition of the two states

$$|\psi\rangle = \alpha\,|0\rangle + \beta\,|1\rangle \tag{1.1}$$

as depicted in Fig 1.1.

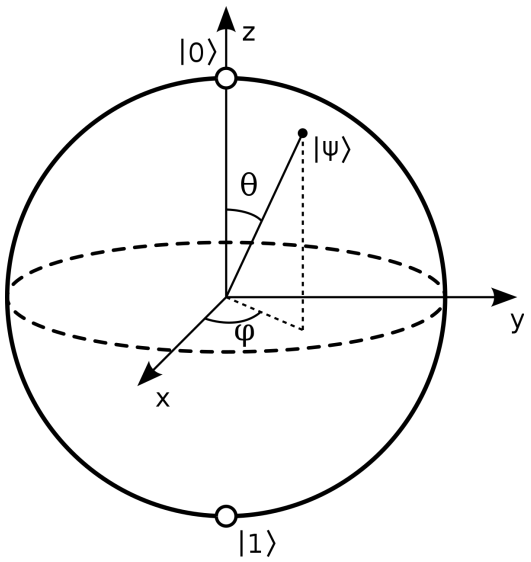

Figure 1.1: A qubit represented in the σ_z eigenstate basis (image taken from Wikipedia). The qubit can be in an "up" state $|0\rangle$, a "down" state $|1\rangle$, or a superposition of the two states $|\psi\rangle$.

If we increase the number of qubits, two qubits can be in a superposition of four states ($|00\rangle$, $|10\rangle$, $|01\rangle$, and $|11\rangle$), and in general N qubits can be in a superposition of 2^N states ($|00...0\rangle$,...,$|11...1\rangle$). Therefore N qubits can be in an arbitrary superposition of up to 2^N different states simultaneously for a given basis, whereas a classical computer that uses binary 0s and 1s can only be in one of these 2^N states at any one time.

Though a benefit of quantum computing is that a string of qubits can simultaneously represent many states, the exponential growth of the qubit state space makes it difficult to explore large quantum systems using a classical computer. Representing the state of an N-qubit system on a classical computer requires the storage of 2^N complex coefficients, for which classical

computers do not have enough memory when N is large. In this thesis, we are motivated by the complexities of large many-body systems and the use of quantum computation for quantum simulation. Specifically, we are concerned with the quantum mechanical phenomenon of *entanglement*, which may be central to understanding complex many-body dynamics.

1.2 Entanglement

Entanglement describes correlations in which the quantum state of each particle in pairs or groups of particles cannot be characterized independently of others. Entanglement can occur between two or more quantum systems separated over large distances, where changes made to one system are immediately correlated with changes in a distant system. For example, consider a system with two subsystems A and B. A general state $|\psi\rangle$ in the system can be represented by the basis vectors of each subsystem such that

$$|\psi_{AB}\rangle = \sum_i \sqrt{\lambda_i} \left|\psi_A^i\right\rangle \otimes \left|\psi_B^i\right\rangle . \tag{1.2}$$

The state is separable (not entangled) if there is only one nonzero λ_i so that $|\psi_{AB}\rangle = |\psi_A\rangle \otimes |\psi_B\rangle$. If there are more than one nonzero λ_i, the state is said to be entangled, and there is entanglement between subsystems A and B.

Understanding entanglement has been identified as potentially crucial for the advancement of quantum information and computing. For example in

the early 1990s, quantum communication protocols such as quantum teleportation and superdense coding were proposed to show how information could be transmitted using qubits. Crucial to both protocols are the use of entangled qubits. The study of entanglement has also been gaining attention as a key bridging between various subfields of physics such as quantum information, quantum statistical mechanics, and condensed matter [1]. Indeed, these three subfields and entanglement are central to this thesis.

1.3 Entanglement Entropy

The importance of entanglement in quantum information motivates us to probe the behavior of quantum systems in relation to entanglement. Much of the literature on this topic has been focused on how entanglement spreads in closed interacting systems that exhibit disorder (a closed system is not in contact with an external system; in an interacting system the particles can interact with each other). Depending on the relative strengths of interactions and disorder, quantum systems often exhibit different behaviors. As a more concrete example, consider a one-dimensional Heisenberg spin chain

$$H = J\sum_{i=1}^{L-1}\left(\sigma_x^i\sigma_x^{i+1} + \sigma_y^i\sigma_y^{i+1} + \sigma_z^i\sigma_z^{i+1}\right) + h\sum_{i=1}^{L} c^i\sigma_z^i \tag{1.3}$$

where σ_x, σ_y, and σ_z are 2×2 Pauli spin matrices. The first summation represents nearest-neighbor interactions and the second summation represents

local magnetic field at each site i. J is the interaction strength, c^i is a random value (from a uniform distribution) on the interval $[-1, 1]$, and h determines the strength of the local magnetic field such that the local magnetic field has random strength in the range $[-h, h]$. In this system the relative values of J and h are important determinants of the system's behavior.

Given such a system, how can we characterize its behavior in relation to entanglement? There have been many different metrics used to explore entanglement in quantum systems including entanglement entropy, Renyi entropy, out-of-time-order correlators, and negativity (all of which are explored in a thesis very relevant to this study [2]). One metric that has historically been particularly well used is entanglement entropy (EE), which is a measure of how much entanglement there is between different systems. To define EE, consider a density matrix $\rho = |\psi\rangle \langle\psi|$ for a state $|\psi\rangle$, which can be partitioned into two subsystems A and B. The bipartite EE is then

$$S_A = -\operatorname{Tr} \rho_A \log \rho_A \tag{1.4}$$

where ρ_A is the reduced density matrix $\rho_A = \operatorname{Tr}_B \rho$. When considering how entanglement spreads in a system, it can be useful to look at the time evolution of S_A, since S_A is a measure of entanglement present in the system. If entanglement spreads differently under certain conditions, then the EE should display unique growth rates for different behaviors of the system.

Indeed there are two categorical behaviors of interest for closed interacting

quantum systems such as Eqn 1.3: thermalization and many-body localization (MBL). Thermalization refers to the rapid spreading of entanglement over the entire system and MBL describes the local retention of entanglement to a small group of particles over long timescales. A thermalized state can be used to erase the initial state of a system and thus "reset" it, while a MBL state can be used to retain initial conditions locally for long times. Thus the two phases are associated with erasure and retention of memory, respectively, which make them attractive concepts for quantum information processing.

1.4 Many-Body Dynamics

It is known that in general, the behavior of a closed interacting 1D quantum system depends on the relative strengths of interactions and disorder [3]. If interaction strength is strong relative to disorder strength, the system will be thermalized, while if interaction strength is weak relative to disorder strength, the system will exhibit MBL [4]. It has also been well studied that a noninteracting system with disorder exhibits Anderson localization (AL) [5]. What follows are brief conceptual explanations of thermalization and localization.

1.4.1 Thermalization

In broad terms, thermalization describes the rapid spreading of local entanglement over the entire system such that the system can be described accurately using quantum statistical mechanics. Quantum thermalization and quantum statistical mechanics have been studied extensively over the past century [6], but most studies have explored the properties of a quantum system in contact with an external reservoir. How, then, does a closed system (one which is not in contact with an external system) thermalize? This can happen when the closed system acts as its own reservoir. Fig 1.2 includes conceptual diagrams helpful for picturing the quantum system [3].

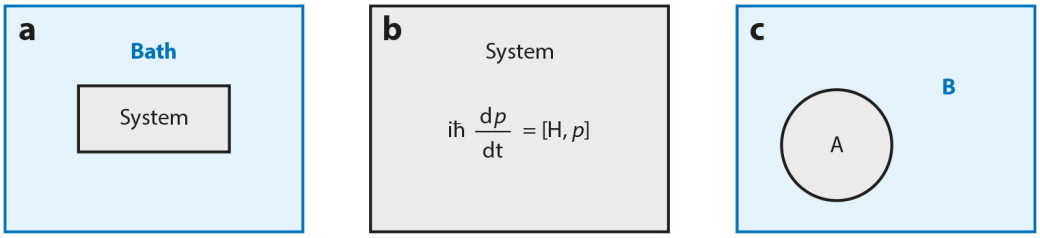

Figure 1.2: Taken from [3]. (a) Traditional treatment of quantum systems in quantum statistical mechanics deals with a system in contact with a reservoir (or bath). (b) In our systems we are concerned with unitary time evolution of the system, i.e. $|\psi(t)\rangle = U|\psi_0\rangle = e^{-iHt}|\psi_0\rangle$. (c) For a closed quantum system, we can picture a subsystem A being in contact with the rest of the system B, which acts as a reservoir for A.

In statistical mechanical terms, subsystem A must contain a small number of degrees of freedom compared to the rest of the system B so that the coupling of A to the rest of the system acts like coupling to a reservoir. The long-time steady states of the subsystems can then obey traditional quantum

thermodynamic and quantum statistical mechanic properties of equilibrium systems. Such a system is said to be thermalized. The spreading of entanglement in a thermal state moves information about the initial state in such a way that it becomes inaccessible over long timescales, which means that a thermal system can "erase" memory of the initial state and thus "reset" the system. In a thermalized system, the entanglement dynamics are characterized by a rapid growth of EE that is linear until it saturates with system size.

1.4.2 Localization

Unlike the rapid growth of entanglement in a thermalized system, a localized system is characterized by a slower growth of entanglement; i.e., entanglement is confined to local groups of particles for long timescales. This is the key feature of localization which distinguishes it from thermalization. The lack of thermalization over reasonable timescales allows for some memory of initial conditions to be retained locally for long times.

In an AL system, although entanglement spreads rapidly within a small group of particles, the presence of disorder inhibits any spread of entanglement beyond some localization length ξ. Since entanglement does not ever spread beyond ξ, the system retains memory of initial conditions even at infinite times. The EE growth of an AL system is characterized by rapid initial growth until localization length ξ, after which there is no more growth so the EE saturates.

In a MBL system, interactions allow entanglement to spread beyond the localization length, but at a much slower rate than in a thermalized system. The slow growth allows for local retention of entanglement and memory over reasonable timescales, although the entanglement will eventually spread through the system at very long times. The entanglement spread in MBL is thus intermediate between thermalization and AL, and is characterized by a logarithmic growth of EE. A general landscape of the important behaviors and some of their properties are displayed in Table 1.1.

Thermalization	Anderson (single particle) localization	Many-body localization
Interactions $\gg$ disorder	No interactions, nonzero disorder	Interactions $\ll$ disorder
Linear EE growth until system size	Rapid EE saturation	Logarithmic EE growth until system size

Table 1.1: Relative strengths of interaction and disorder and characteristic EE growth rates for the different phases.

1.5 Overview

Although EE has been used extensively to quantify entanglement, a criticism of EE is that it provides only a single number to represent complicated

dynamics. Recently, new metrics based on quantum statistical mechanics have been developed that focus on spectral distributions to characterize entanglement in a system. Of these metrics, two are addressed in this study: the Eigenstate Entanglement Spectrum (EES) and Entanglement Spectrum Statistics (ESS). However, these metrics have generally only been used to study well-known spin-1/2 chains such as the Heisenberg and Ising spin chains [7, 8, 9]. These model systems can be difficult to recreate experimentally, so our theoretical work is motivated by a desire to explore a system that is experimentally accessible. In this thesis, we use the EES and ESS to study a class of nearest-neighbor coupled spin-1/2 chain Hamiltonians that can be experimentally accessed in a solid state NMR system.

The body of this thesis begins in Section 2 with a derivation and explanation of the Hamiltonian of study, which can be modeled using a solid state NMR system. This is followed by an overview of entanglement metrics including EE, EES, and ESS in Section 3. In section 4, results and discussion of EES and ESS data are presented. The appendices include further details about methodology and many-body dynamics.

Chapter 2

NMR Engineered Hamiltonian

The theoretical system studied is a one-dimensional nearest-neighbor coupled spin chain based on a physical system that is experimentally accessible using solid state NMR (SSNMR). A derivation of the Hamiltonian will begin with an explanation of the properties of the physical system followed by how the physical system determines the theoretical system.

2.1 Insulator in NMR

Nuclear magnetic resonance (NMR) is a phenomenon of nonzero-spin nuclei in which they absorb and re-emit electromagnetic radiation at their natural resonant frequency. NMR spectroscopy utilizes this property to observe signals of local magnetic fields around nuclei. The advantage of NMR spectroscopy is therefore that it gives information about physical processes at the

atomic level [10]. A sample to be used for NMR measurement is first placed in a strong constant external magnetic field $\vec{B}_0$ to polarize the nuclear spins in the direction of $\vec{B}_0$. The nuclei can then be excited by radiofrequency (RF) pulses of a transverse field $\vec{B}_1$, which induces a NMR response (free induction decay). As the sample relaxes to its thermal equilibrium state, the transverse magnetization is measured.

In the presence of external magnetic field $\vec{B}_0$, a spin nucleus experiences Zeeman splitting, in which energy levels of the spin become split according to spin orientation. This occurs because the external field exerts a torque on the spin nucleus with potential energy $U = \gamma \vec{S} \cdot \vec{B}_0$ where γ is the gyromagnetic ratio of the nucleus and $\vec{S} = \frac{1}{2}\vec{\sigma}$ with $\hbar = 1$. The potential energy value varies according to $\vec{S}$, which results in different energy levels for different spin orientations. If $\vec{B}_0 = B_0 \hat{z}$, the spin precesses about the z axis at the Larmor frequency $\omega_0 = \gamma B_0$. The nuclear Zeeman Hamiltonian for a system of N spins placed in an external magnetic field is then

$$H_Z = \omega_0 \sum_{i=1}^{N} S_z^i \tag{2.1}$$

where we use the shorthand $\sigma_n^i = \mathbb{1}^{\otimes(i-1)} \otimes \sigma_n \otimes \mathbb{1}^{\otimes(L-i-1)}$ (i.e. σ_n^i represents the operator σ_n acting only on the i-th spin).

In addition to each spin coupling with the external magnetic field, the spins can also interact with each other. The spins interact via dipolar cou-

pling, for which the full interaction between two spins i and j is

$$H_D = \frac{\mu_0 \gamma^2}{4\pi r_{ij}} \left[\vec{S}_i \cdot \vec{S}_j - \frac{3(\vec{S}_i \cdot \vec{r}_{ij})(\vec{S}_j \cdot \vec{r}_{ij})}{r_{ij}^2} \right]. \tag{2.2}$$

For large external magnetic fields, the strength of the dipolar coupling is much weaker than the Zeeman interaction, so we can treat the dipolar coupling as a small perturbation to the Zeeman Hamiltonian. This allows us to use perturbation theory to keep only the parts that commute with the Zeeman term. The truncated interaction term (see e.g. Section 3.1 of [10] for a derivation) is

$$H_D^{ij} = \omega_D^{ij} \left(3S_z^i S_z^j - \vec{S}^i \cdot \vec{S}^j \right) \tag{2.3}$$

where ω_D^{ij} is the interaction strength between spins i and j. The interaction strength is given by

$$\omega_D^{ij} \propto \frac{3\cos^2\theta_{ij} - 1}{|r_i - r_j|^3} \tag{2.4}$$

where θ_{ij} and $|r_i - r_j|$ are shown in Fig 2.1 as θ and r. This truncated dipolar interaction term is known as the secular dipolar interaction term, since it is approximated as a first order perturbation to the Zeeman term for a strong B_0. The total Hamiltonian for an insulating crystal in a strong external field B_0 includes Zeeman and dipolar interactions:

$$H_{tot} = H_Z + H_D = \omega_0 \sum_i S_z^i + \sum_{i<j} \omega_D^{ij} \left(3S_z^i S_z^j - \vec{S}^i \cdot \vec{S}^j \right). \tag{2.5}$$

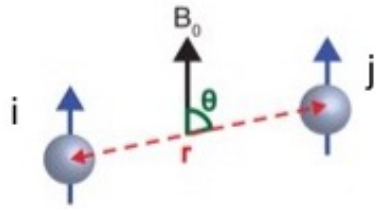

Figure 2.1: For two interacting particles i and j, the angle θ and distance $r = |r_i - r_j|$ determine the secular dipolar coupling strength.

2.2 Fluorapatite

Although the Hamiltonian in Eqn 2.5 provides a clean theoretical framework, three-dimensional systems are difficult to work with numerically because dynamics can be highly complex. One way to make the system simpler while keeping it grounded in a physical system is to model the Hamiltonian on a system that can approximate a one-dimensional chain.

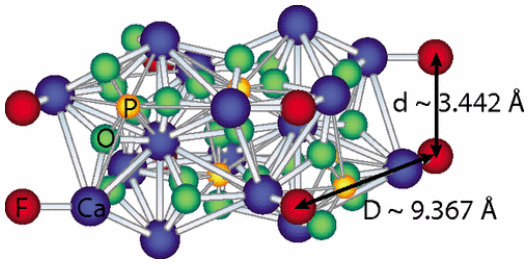

Figure 2.2: Fluorapatite (FAP) crystal representation taken from [11]. Dipolar interactions make intra-chain NN interactions about 40 times stronger than cross-chain NN interactions and 8 times stronger than intra-chain NNN couplings. This allows us to neglect cross-chain interactions and approximate the crystal as a one-dimensional NN coupled spin chain system.

In this study, fluorapatite (FAP) is the basis for such an approximation.

FAP consists of a series of chains of spin-1/2 fluorine nuclei that are surrounded by other nuclei, such as spin-1/2 phosphorous nuclei. The fluorine nuclei interact via dipolar coupling, the strength of which in a strong external field is given by Eqn 2.4. As shown in Fig 2.2, the distance between NN fluorine nuclei within the same chain is about 3.4 Å and the distance between NN nuclei in different chains is about 9.4 Å. The longer distance to neighboring nuclei across a chain compared to neighboring nuclei within a chain allow us to approximate the system as an ensemble of noninteracting chains.

If we consider cross-chain interactions between the two closest cross-chain nuclei, the coupling strength is significantly weaker than for two adjacent intra-chain nuclei. NN cross-chain nuclei have an angle $\theta \approx 0$ between them in addition to the $1/r^3$ drop off. Since the distance for intra-chain NN is about 2.75 that of cross-chain NN, intra-chain NN interactions are about $2.75^3 \times (3\cos^2(0) - 1) \approx 40$ times stronger than cross-chain NN interactions. Within a chain, the distance for NNN is twice that of NN, so NN dipolar interactions are $2^3 = 8$ times stronger than NNN dipolar interactions ($\theta = \pi/2$ for intra-chain interactions). Therefore, for FAP,

$$\frac{\omega_D^{(in)}}{\omega_D^{(cross)}} \approx 40 \quad \text{and} \quad \frac{\omega_D^{(NN)}}{\omega_D^{(NNN)}} = 8. \tag{2.6}$$

Consequently, cross-chain NN and intra-chain NNN interactions can be neglected (in addition to all other longer distance interactions) to approximate

the FAP system as an ensemble of noninteracting 1D NN coupled spin chains. The dipolar Hamiltonian for the FAP system can then be rewritten as

$$H_D = \omega_D \sum_{i=1}^{L-1} \left(3S_z^i S_z^{i+1} - \vec{S}^i \cdot \vec{S}^{i+1} \right) \tag{2.7}$$

for a chain of L spins, which is valid for short time periods. The interaction strength ω_D can be pulled out of the summation since it is constant for each intra-chain NN interaction.

2.3 Total Hamiltonian

In the experimental system, the Hamiltonian in Eqn 2.7 can be further modified using coherent averaging techniques [11]. These are periodic trains of radio frequency (RF) pulses that are used to create different effective Hamiltonians. One example of such a Hamiltonian is the double quantum Hamiltonian (H_{DQ})

$$H_{DQ} = \omega_D \sum_{i=1}^{L-1} \left(S_x^i S_x^{i+1} - S_y^i S_y^{i+1} \right). \tag{2.8}$$

H_{DQ} is a well-studied integrable system which maps to a free-fermionic model under a Jordan-Wigner transformation [12]. Coherent averaging techniques also allow the refocusing of spin-1/2 phosphorous nuclei that surround the fluorine chains to add local disorder to the system. Since the FAP crystal and SSNMR system are kept at high (room) temperature such that $\hbar\omega_0^{(P)} \ll k_B T$, the spins of the phosphorous nuclei are distributed in a random configuration.

The refocusing of these phosphorous spins add local randomness, or disorder, to the fluorine chains.

Thus using coherent averaging techniques and the phosphorous nuclei, it is possible to create an effective Hamiltonian of the form [11]

$$H = J\sum_{i=1}^{L-1}\left[\frac{u+v}{2}\sigma_x^i\sigma_x^{i+1} + \frac{v-u}{2}\sigma_y^i\sigma_y^{i+1} - v\sigma_z^i\sigma_z^{i+1}\right] + \sum_\alpha g_\alpha \sum_{i=1}^{L} c_\alpha^i \sigma_\alpha^i \quad (2.9)$$

where J sets the overall interaction strength scale, u and v together set the energy scale, g_α sets the disorder strength in the direction α, and $c_\alpha^i \in [-1, 1]$ is a random value that represents local disorder. In the first summation, the first two terms map to a non-interacting fermionic system. When v is nonzero, the third term introduces interactions. If $u = 1$ and $v = 0$, the Hamiltonian reduces to

$$H = \frac{J}{2}\sum_{i=1}^{L-1}\left[\sigma_x^i\sigma_x^{i+1} - \sigma_y^i\sigma_y^{i+1}\right] + \sum_\alpha g_\alpha \sum_{i=1}^{L} c_\alpha^i \sigma_\alpha^i \quad (2.10)$$

which is just H_{DQ} with disorder. On the other hand if we set $u = 0$ and $v = 1$, the Hamiltonian reduces to

$$H = \frac{J}{2}\sum_{i=1}^{L-1}\left[\sigma_x^i\sigma_x^{i+1} + \sigma_y^i\sigma_y^{i+1} - 2\sigma_z^i\sigma_z^{i+1}\right] + \sum_\alpha g_\alpha \sum_{i=1}^{L} c_\alpha^i \sigma_\alpha^i \quad (2.11)$$

which is the secular dipolar Hamiltonian of Eqn 2.7 with disorder. The next chapter describes two entanglement metrics used to explore the features of this class of Hamiltonians.

Chapter 3

Metrics

This chapter features detailed descriptions of our metrics for characterizing entanglement. The chapter begins with a general discussion of entanglement and information, and then moves on to define entanglement entropy and entanglement spectra as useful metrics of entanglement and information. Lastly, the two metrics used in this study are introduced: the eigenstate entanglement spectrum and eigenstate spectrum statistics.

In order to understand the importance of entanglement as a metric for information, it is instructive first to consider the density matrix of a system. The general definition of a density matrix is

$$\rho = \sum_i p_i \left|\psi_i\right\rangle \left\langle\psi_i\right| \tag{3.1}$$

where each $|\psi_i\rangle$ is a possible state of the system and p_i is the probability

associated with that state. If we are given a pure state $|\psi\rangle$, the density matrix is simply $\rho = |\psi\rangle\langle\psi|$ where $p_i = 1$, so we know with certainty that the system is in state $|\psi\rangle$. However, if we have a mixed state, then there are more than one p_i, so there is uncertainty about the exact state of the system. Thus a pure state represents complete knowledge about the state of the system, whereas a mixed state represents a lack of knowledge about the system.

We use this idea of the density matrix as a representation of information to connect entanglement and information. To do this, we consider the reduced density matrix of a bipartite system. A general pure state in a bipartite system can be represented as $|\psi_{AB}\rangle = \sum_i \sqrt{\lambda_i}\,|\psi_A^i\rangle \otimes |\psi_B^i\rangle$, which is a decomposition of the state into a sum of tensor products of basis vectors from each subsystem, A and B (the Schmidt decomposition). The system is in a separable state (not entangled) if there is only one nonzero λ_i, so $|\psi_{AB}\rangle = |\psi_A\rangle \otimes |\psi_B\rangle$. On the other hand, it is entangled if there are more than one nonzero λ_i.

Now we consider the reduced density matrix of a separable state and an entangled state. If we partition a system in the state ρ into subsystems A and B, the reduced density matrix of subsystem A is defined as

$$\rho_A = \mathrm{Tr}_B\,\rho \tag{3.2}$$

where Tr_B is a partial trace over subsystem B. For a separable state, the

reduced density matrix is then

$$\rho_A = \mathrm{Tr}_B \left(|\psi_{AB}\rangle \langle \psi_{AB}| \right) = \mathrm{Tr}_B \left(|\psi_A\rangle \langle \psi_A| \otimes |\psi_B\rangle \langle \psi_B| \right) = |\psi_A\rangle \langle \psi_A| . \quad (3.3)$$

This is a pure state in subsystem A, which represents complete knowledge about subsystem A. For an entangled state, the reduced density matrix is

$$\rho_A = \mathrm{Tr}_B \sum_{ij} \sqrt{\lambda_i}\sqrt{\lambda_j} \left(\left|\psi_A^i\right\rangle \left\langle \psi_A^j \right| \otimes \left|\psi_B^i\right\rangle \left\langle \psi_B^j \right| \right) \quad (3.4)$$

where the partial trace over subsystem B forces $i = j$ due to orthogonality, so we are left with

$$\rho_A = \sum_i \lambda_i \left|\psi_A^i\right\rangle \left\langle \psi_A^i \right| . \quad (3.5)$$

This is a mixed state in subsystem A, which represents a lack of knowledge about subsystem A. Thus when there is entanglement between subsystems A and B, tracing out (throwing away information about) subsystem B causes a loss of information in subsystem A. The following entanglement metrics, which all depend on the the reduced density matrix of a bipartite system, are of interest to quantum information for this very connection between entanglement and information.

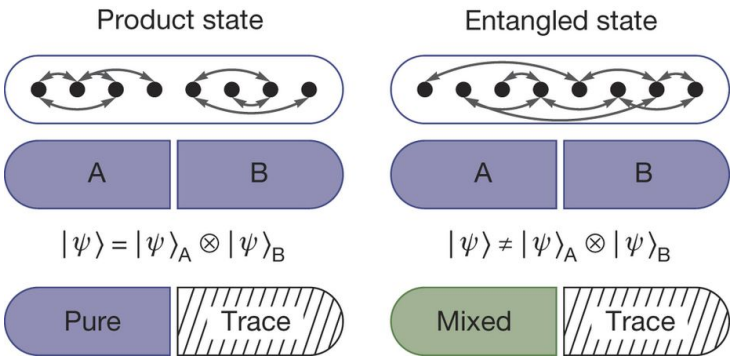

Figure 3.1: A representation of the reduced density matrices for separable (product) and entangled states, taken from [13].

3.1 Entanglement Entropy

The first metric introduced is Bipartite Entanglement Entropy (EE). It is defined as

$$S = -\operatorname{Tr} \rho_A \log \rho_A \tag{3.6}$$

where ρ_A is the reduced density matrix introduced above. EE is therefore the negative trace of the von Neumann entropy of subsystem A. It is an indication of how much entanglement there is between subsystems A and B, which can be demonstrated by computing the EE for a separable state and an entangled state.

For a separable state $|\psi_{AB}\rangle = |\psi_A\rangle \otimes |\psi_B\rangle$, the reduced density matrix is a pure state in subsystem A so the EE is $S = -\sum_i (1)(\ln 1) = 0$. For an entangled state, the reduced density matrix is a mixed state in subsystem A so the EE is nonzero: $S = -\sum_i (\lambda_i)(\ln \lambda_i) \neq 0$. Thus zero EE signifies a

lack of entanglement between subsystems A and B, whereas a nonzero value indicates how much entanglement there is.

3.2 The Entanglement Spectrum

Unlike the EE which expresses the level of entanglement as a number, the entanglement spectrum looks at the spectrum of eigenvalues of a reduced density matrix to study entanglement dynamics. More precisely, the general methodology is to define a reduced density matrix

$$\rho_A = \sum_i \lambda_i \left|\psi_A^i\right\rangle \left\langle\psi_A^i\right| \tag{3.7}$$

from which the eigenvalues λ_i are extracted and sorted to be used as spectral values. Taking the spacings between these spectral values can offer insight into how the system is behaving. For example, it is well documented that for nonintegrable systems, spectral values locally repel each other in order to avoid level crossing. On the other hand, for highly ordered and symmetric systems, there tend to be high levels of degeneracies and thus many λ_i have similar values. Therefore, if we zoom in on a small window of eigenvalues, the spacings between adjacent levels $\Delta\lambda_i = \lambda_i - \lambda_{i-1}$ can be indicative of the integrability of the system. Low spacing values imply high levels of degeneracy and thus order, while high spacing values indicate high level repulsion and thus chaos. These spacings have been shown to follow several types of

distributions depending on the level of disorder and symmetries conserved in the system. The distributions of interest are based on Random Matrix Theory (RMT) ensembles that have been used extensively to describe energy level statistics of various systems. More detail about these distributions is provided in Section 3.2.2.

3.2.1 Spacings and Ratios

Spacings of adjacent spectral values are a useful metric to characterize how spectrum levels are distributed in the system of interest. The disadvantage of spacings, however, is that the spectra are sensitive to local level density fluctuations. Therefore in order to correlate spectral results with RMT distributions, the original spectra must be unfolded to remove the influence of the level density (see Appendix A for more detail). A potentially useful alternative to this problem is to look at ratios of adjacent spacings.

In [9], the spectrum values are used to find ratios of adjacent spacings, defined as

$$r_i = \frac{(\lambda_{i-1} - \lambda_i)}{(\lambda_i - \lambda_{i+1})} = \frac{s_{i-1}}{s_i} \tag{3.8}$$

for spectral values λ_i. These ratios of adjacent spacings may not require unfolding for slowly varying level densities (Appendix A). In recent literature, however, the definition of ratios proposed in [8] has been the most popular

method used. This definition of ratios is

$$r_i = \frac{\min(s_i, s_{i-1})}{\max(s_i, s_{i-1})} \tag{3.9}$$

which supposedly does not require unfolding because ratios of consecutive level spacings (with this definition) are independent of the local density of states [14].

3.2.2 Distributions

The following four distributions are of particular interest to our study: Poisson, Semi-Poisson, Gaussian Orthogonal Ensemble (GOE), and Gaussian Unitary Ensemble (GUE) (see Fig 3.2). The spectrum value spacings distributions can be characterized to a very good approximation by a single equation (the Wigner surmise modified to interpolate the four distributions) [7, 14, 15]:

$$P(s) = C_1(\gamma, \alpha) s^{\alpha} e^{C_2(\gamma,\alpha) s^{2-\gamma}} \tag{3.10}$$

where

$$C_2(\gamma, \alpha) = \left(\frac{\Gamma\left(\frac{2+\alpha}{2-\gamma}\right)}{\Gamma\left(\frac{1+\alpha}{2-\gamma}\right)} \right)^{2-\gamma} \quad \text{and} \quad C_1(\gamma, \alpha) = \frac{(2-\gamma) C_2^{\frac{1+\alpha}{2-\gamma}}}{\Gamma\left(\frac{1+\alpha}{2-\gamma}\right)} \tag{3.11}$$

are normalization constants that satisfy $\langle s \rangle = 1$. The parameter $1 \geq \gamma \geq 0$ controls the tails of the distributions and thus level rigidity, while $2 \geq \alpha \geq 0$

determines the level repulsion. Poisson statistics correspond to $\gamma = 1$ and $\alpha = 0$, GOE to $\gamma = 0$ and $\alpha = 1$, and GUE to $\gamma = 0$ and $\alpha = 2$. For this study, semi-Poisson statistics corresponding to $\gamma = \alpha = 1$ is also of relevance. Thus we have four important distributions that can be interpolated using a single equation.

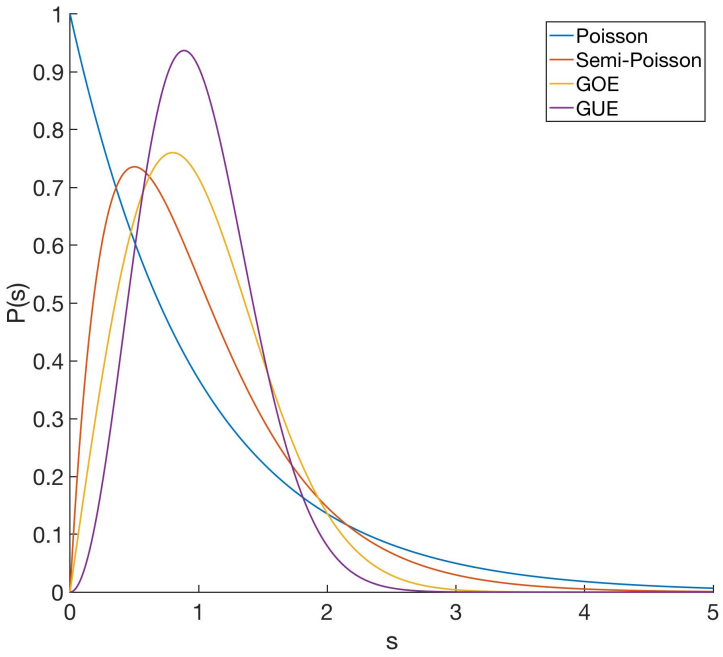

Figure 3.2: Spacing distributions of the four ensembles of interest: Poisson, Semi-Poisson, GOE, and GUE.

For this study, we would also like to be able to describe the distributions using spectrum value ratios rather than spacings. Though we can interpolate between the four distributions with a generic equation, it requires a rather large number of parameters, so instead we separate Poisson statistics from

Gaussian statistics. The (semi-)Poisson distributions in terms of ratios are described by

$$P(r) = A_\alpha \frac{r^\alpha}{(1+r)^{2\alpha+2}} \tag{3.12}$$

and the Gaussian distributions by

$$P(r) = \frac{1}{Z_\beta} \frac{(r+r^2)^\beta}{(1+r+r^2)^{\frac{3}{2}\beta+1}} \tag{3.13}$$

where A_α and Z_β are normalization constants [9, 14]. Fig 3.3 depicts the distributions for ratios.

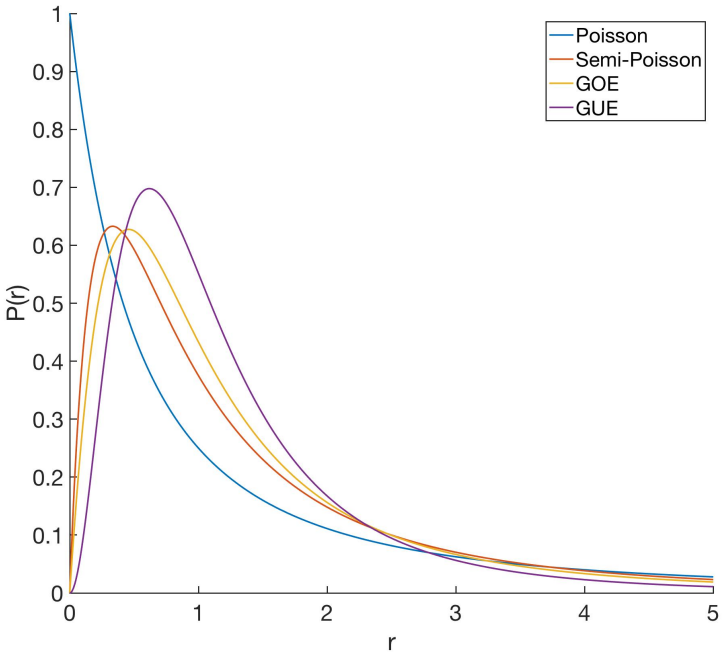

Figure 3.3: Ratio distributions of the four ensembles of interest: Poisson, Semi-Poisson, GOE, and GUE.

Depending on the metric used, the different distributions may signify slightly different behaviors of the system. These distributions have been used historically to characterize system behaviors using energy level distributions. In general Poisson behavior signifies little level repulsion and high degeneracy, which has been used as an indicator of integrability. On the other hand, Gaussian ensembles have greater level repulsion and low levels of degeneracy, so Gaussian ensembles have been associated with chaotic, nonintegrable systems. Recently, these ideas have been applied to eigenvalue level distributions of entanglement spectra.

Of the two Gaussian ensembles used here, GUE has more level repulsion than GOE, which is consistent with statistics switching from GOE to GUE when additional symmetries are broken. A switch from GOE to GUE is often associated with the breaking of time reversal symmetry [9], but statistics can remain GOE even if time reversal symmetry is broken as long as certain other symmetries are conserved [16]. Semi-Poisson behavior falls in between Poisson and Gaussian statistics in terms of chaoticity. It is therefore tempting to say, generally, that localized systems obey (semi-)Poisson statistics, while thermalized systems obey Gaussian statistics [7, 9].

For our two metrics in this study, the EES and ESS, we apply the general concepts of the entanglement spectrum to two different reduced density matrices. In the EES, the reduced density matrix is defined according to an eigenstate of the Hamiltonian, while in ESS it is defined according to a random initial product state that has been time evolved. Following literature

about the two metrics, for the EES we use min/max ratios of Eqn 3.9 [7] and for ESS the simple ratios of Eqn 3.8 [9].

3.3 Eigenstate Entanglement Spectrum

The Eigenstate Entanglement Spectrum (EES) is obtained by finding an eigenvector of the Hamiltonian H, Schmidt decomposing the eigenvector, and then taking the logarithm of the Schmidt coefficients. The resulting values are used to compute min/max ratios.

3.3.1 Methods

What follows is a more detailed explanation, following [7]. We first start with an eigenstate of the Hamiltonian, $|\psi_i\rangle$, for which $H|\psi_i\rangle = E_i|\psi_i\rangle$. The reduced density matrix is then defined as $\rho_A = \mathrm{Tr_B}\rho = \mathrm{Tr_B}|\psi_i\rangle\langle\psi_i|$ where we partition the system into two subregions A and B. Taking the logarithm of ρ_A, we can define the "entanglement Hamiltonian" $H_{\mathrm{ent,A}} = -\ln\rho_A$. For the EES, the spectral values are the eigenvalues of the entanglement Hamiltonian.

The motivation for defining the entanglement Hamiltonian as a logarithm is rooted in studying the energies of a system in thermal equilibrium. The reduced density matrix of such a system is

$$\rho_A^{(eq)} = \sum_i e^{-\beta\epsilon_i}|A_i\rangle\langle A_i| \tag{3.14}$$

where ϵ_i are the energy levels of corresponding eigenstates $|A_i\rangle$ and $\beta = 1/k_BT$. We can set $\beta = 1$ since T is constant throughout the system in thermal equilibrium and any nonzero value of β does not change spectral dynamics. Then to use the energy levels ϵ_i as the spectral values, we must take the logarithm to get

$$H_{ent,A}^{(eq)} = -\ln \rho_A^{(eq)} = \sum_i \epsilon_i \left|A_i\right\rangle \left\langle A_i\right| . \tag{3.15}$$

Now ϵ_i are the eigenvalues that can be used to compute spacings or ratios.

The above description provides a clean conceptual definition for the spectral values, but it can be numerically more convenient to determine the same spectrum values from the coefficients of a Schmidt decomposition. The Schmidt decomposition of $|\psi\rangle$ is defined as $|\psi\rangle = \sum_i c_i \left|A_i\right\rangle \otimes \left|B_i\right\rangle$, which essentially states that any vector $|\psi\rangle$ can be expressed as a superposition of tensor product states of corresponding basis vectors from subregions A and B (note that if there are more than one nonzero c_i, the state is entangled). For the EES, we define $c_i = e^{-\zeta_i/2}$ and the ζ_i values determined from this Schmidt decomposition constitute our spectrum (hereby referred to as the "Schmidt spectrum"). We can use Schmidt coefficients as spectral values instead of eigenvalues of the entanglement Hamiltonian because the two are equivalent (up to a possible scalar factor).

To explain the connection between Schmidt coefficients and eigenvalues of ρ_A, we use the Schmidt decomposition of a state $|\psi\rangle = \sum_i c_i \left|A_i\right\rangle \otimes \left|B_i\right\rangle$

to write the density matrix $\rho = |\psi\rangle\langle\psi|$ as

$$\rho = \sum_{i,j} c_i c_j^* \left(|A_i\rangle \otimes |B_i\rangle\right)\left(\langle A_j| \otimes \langle B_j|\right) = \sum_{i,j} c_i c_j^* \left(|A_i\rangle\langle A_j| \otimes |B_i\rangle\langle B_j|\right). \tag{3.16}$$

Now if we take the partial trace over subregion B to get the reduced density matrix ρ_A, the trace acts only on the terms with B basis vectors in it, i.e.

$$\rho_A = \sum_{i,j} c_i c_j^* \left(|A_i\rangle\langle A_j|\right)\left(\mathrm{Tr_B}\,|B_i\rangle\langle B_j|\right). \tag{3.17}$$

Let us examine the partial trace over B more closely. It is defined as

$$\sum_k \langle B_k|\left(|B_i\rangle\langle B_j|\right)|B_k\rangle = \sum_k \langle B_k|B_i\rangle\langle B_j|B_k\rangle \tag{3.18}$$

where B_k are also basis vectors of subregion B. Since inner products are simply scalars, we can rewrite them in reverse order as

$$\sum_k \langle B_j|B_k\rangle\langle B_k|B_i\rangle = \sum_k \langle B_j|\left(|B_k\rangle\langle B_k|\right)|B_i\rangle. \tag{3.19}$$

We can then pull B_i and B_j out of the summation since they do not depend on k to get

$$\langle B_j|\left(\sum_k |B_k\rangle\langle B_k|\right)|B_i\rangle = \langle B_j|B_i\rangle \tag{3.20}$$

where we use the property that the trace of a density matrix is required to be unity, $\sum_k |B_k\rangle\langle B_k| = 1$. Since the Schmidt decomposition is defined in

terms of basis vectors, which are orthonormal, we know that $\langle B_j|B_i\rangle = \delta_{i,j}$. Plugging this back into Eqn 3.17, this forces $i = j$ so we end up with

$$\rho_A = \sum_i c_i^2 \left|A_i\right\rangle \left\langle A_i\right| \tag{3.21}$$

which is just the normal definition of a reduced density matrix. The coefficients c_i of the Schmidt decomposition squared therefore give us the diagonal values of ρ_A. The eigenvalues of the "entanglement Hamiltonian" $H_{\text{ent,A}} = -\ln \rho_A$ are then simply $\{-\ln c_i^2\}$. For the EES we define the Schmidt decomposition coefficients as $c_i = e^{-\zeta_i/2}$, so we get $\{\zeta_i\}$ for our eigenvalue spectrum (the Schmidt spectrum). Notice the similarity to the ϵ_i of a system in thermal equilibrium.

Finally, once the spectral values have been extracted, we can compute ratios for the EES [8], which are defined as

$$r_i = \frac{\min(s_i, s_{i-1})}{\max(s_i, s_{i-1})}. \tag{3.22}$$

3.3.2 Validation

The ESS was used in [7] to study a a Heisenberg spin chain

$$H = \sum_{\alpha=x,y,z} \left[J \sum_{i=1}^{N} \left[S_\alpha^i S_\alpha^{i+1} \right] + h_\alpha \sum_{i=1}^{N} c_\alpha^i S_\alpha^i \right] \tag{3.23}$$

where $S^i_\alpha = \frac{1}{2}\sigma^i_\alpha$, h_α sets the maximum disorder strength, and c^i_α is a random value on the interval $[-1, 1]$. In the results it is reported that GOE or GUE indicate thermalization (depending on symmetries present) and Semi-Poisson indicates MBL. Figure 3.4 shows the figures reported in [7] for spacings of unfolded Schmidt spectrum values. The figures show spectrum spacings for both GOE and GUE. Data are included for 14 and 18 spins, both of which are partitioned in the middle of the chain. The data was obtained by averaging over eigenstates of the middle third of the energy spectrum to reduce statistical fluctuations. The middle third was picked because the level density varies least in that region (see A for more detail). For a large spin system, averaging would not be necessary for better statistics since a single eigenstate would be described by more Schmidt coefficients.

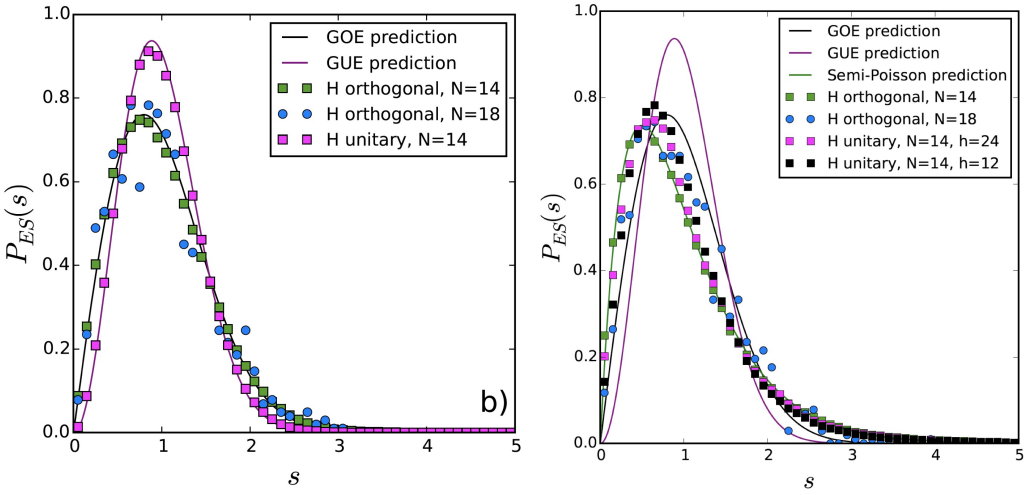

Figure 3.4: Eigenstate entanglement spectra reported in [7] for thermal (left) and local (right) regimes for spin chains of length 14 and 18. For orthogonal thermal, $h_x = h_z = .25$, $h_y = 0$; for orthogonal local, $h_x = h_z = 12$, $h_y = 0$.

In order to test that our methodology was correct, we attempted to generate the same data for the same Hamiltonian. Figure 3.5 shows data generated for thermal and MBL phases for 14 spins with a partition along the middle and a similar average over the middle third of the energy spectrum. The thermal phase exhibits GOE statistics and the MBL phase exhibits SP statistics, as expected.

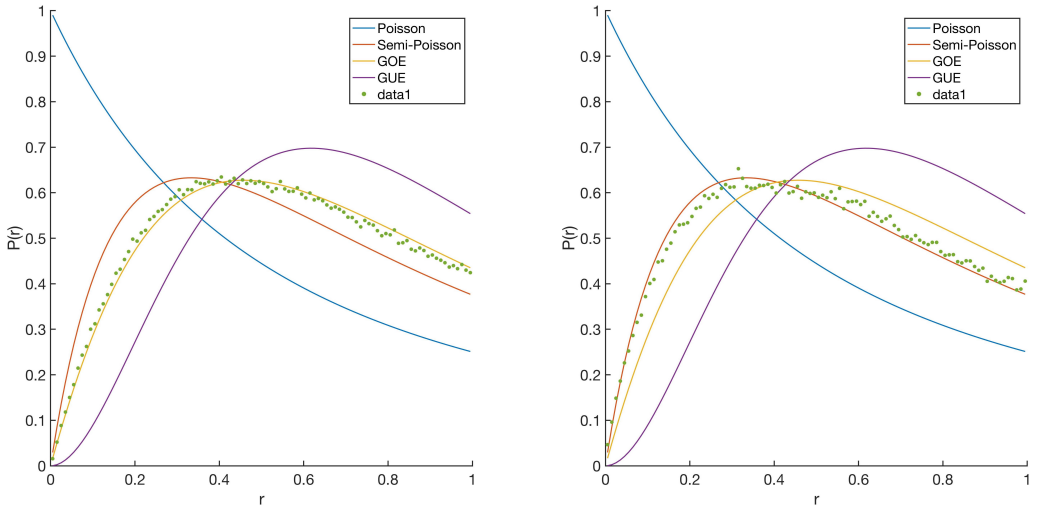

Figure 3.5: Eigenstate entanglement spectra generated for thermal (left) and MBL (right) regimes for 14 spins. For orthogonal thermal, $h_x = h_z = .25$, $h_y = 0$; for orthogonal local, $h_x = h_z = 12$, $h_y = 0$. Data are displayed as ratios rather than spacings.

In Fig 3.5 the data are plotted using the min/max ratio method of ratios rather than unfolded spacing values because min/max ratios are cleaner and easier to work with. Though not shown, we also looked at unfolded spacings and unitary symmetry classes as well. In all cases, the data matched the distributions reported in [9]. The agreement of the methodology with the

results of the paper suggest that the methods are correct.

3.4 Entanglement Spectrum Statistics

Entanglement Spectrum Statistics (ESS) are obtained by time evolving a random product state under the Hamiltonian H, then computing the reduced density matrix of the time evolved state, and then extracting eigenvalues from the reduced density matrix.

3.4.1 Methods

What follows is a more detailed explanation, based the methods in [9]. The system is first initialized in a random factorized state $|\Psi_0\rangle = \otimes_j |\psi\rangle_j$ with $|\psi\rangle_j = e^{i\phi_j} cos(\theta_j) |0\rangle_j + e^{i\chi_j} sin(\theta_j) |1\rangle_j$. That is, each spin in the chain is initialized at a random point on the Bloch sphere. The parameters $\theta_j,\ \phi_j,\ \chi_j\ \in [0, 2\pi]$ are initialized with uniform probability. Though it seems redundant to use two phase angles with this range, we use the same methodology as [9] since it does not affect the overall physics. The initial state is factorable to ensure that there is no entanglement present; we can then try to understand how entanglement spreads in the system as time progresses.

The initial density matrix is given by $\rho_0 = |\Psi_0\rangle \langle\Psi_0|$. We can time evolve the density matrix with a unitary operator $U = e^{-iHt}$, so $\rho(t) = U\rho_0 U^\dagger$. This is the equivalent of time evolving the initial state since $|\Psi(t)\rangle = e^{-iHt} |\Psi_0\rangle$, which gives $\rho(t) = |\Psi(t)\rangle \langle\Psi(t)|$. Next, we determine the reduced density

matrix $\rho_A(t) = \mathrm{Tr_B}[\rho(t)]$ of the left side of the chain and extract the eigenvalues of $\rho_A(t)$, ordered in decreasing order and denoted by $\{p_i\}_{i=1}^{2^{N/2}}$. These eigenvalues of the time-evolved reduced density matrix constitute our "eigenvalue spectrum" for ESS. We can then compute ratios of consecutive spacings $r_i = (p_{i-1} - p_i)/(p_i - p_{i+1})$.

Due to randomization of the initial state and local disorder values, each generation of ESS data begins at a different initial state and evolves under a different Hamiltonian. Therefore, we perform many iterations over initial states and disorder values to reduce statistical fluctuations. In creating the final plots, we generate a histogram using the eigenvalue ratios from all of these iterations. We then normalize the histogram, essentially creating a histogram of the average of eigenvalue ratios.

3.4.2 Validation

ESS has been used to explore an anisotropic Heisenberg spin chain [9]

$$H = J \sum_{i=1}^{L-1} \left(\sigma_x^i \sigma_x^{i+1} + \sigma_y^i \sigma_y^{i+1} + \Delta \sigma_z^i \sigma_z^{i+1} + z^i \sigma_z^i + x^i \sigma_x^i \right) \tag{3.24}$$

where Δ gives the interaction strength and z^i and x^i give the maximum values of random local magnetic field strength on the intervals $[-z^i, z^i]$ and $[-x^i, x^i]$. For this Hamiltonian, a Poisson distribution is reported for Anderson localization, a GUE distribution for thermalization (or GOE depending on symmetries present), and a non-universal distribution that approaches

GUE when the largest singular values are discarded for MBL [9]. Figure 3.6 shows the plots in [9] depicting the different distributions for the three different regimes.

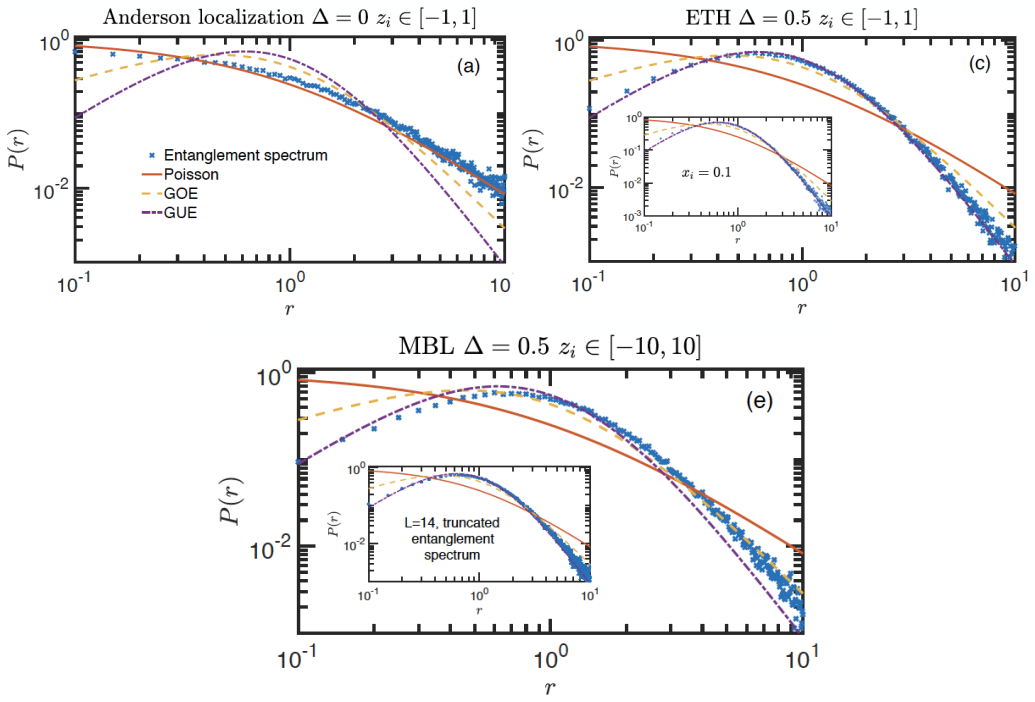

Figure 3.6: ESS reported for Anderson localization (top left), thermalization (top right), and MBL (bottom) regimes for 12 spins [9]. For Anderson localization, interactions Δ are set to zero and disorder strength z_i is a random value in the range $[-1, 1]$ (though in principle any disorder value produces AL). $\Delta = .5$ and $z_i \in [-1, 1]$ give a thermal distribution and $\Delta = .5$ and $z_i \in [-10, 10]$ give a MBL distribution.

In order to test that my methodology was correct, I attempted to generate the same data for the same Hamiltonian. Figure 3.7 shows data generated for the three regimes for 12 spins, a partition in the middle of the chain, and $t = 1000\frac{1}{J}$. The methodology of [9] reports "2000 realizations of disorder,"

which makes it slightly unclear whether they performed 2000 Hamiltonians for a single initial product state or also averaged over several product states. For my validation data, I generate 40 initial random product states and 50 Hamiltonians for each initial state to get a total of 2000 realizations. Fig 3.7 depicts the plots I generated for the same parameters.

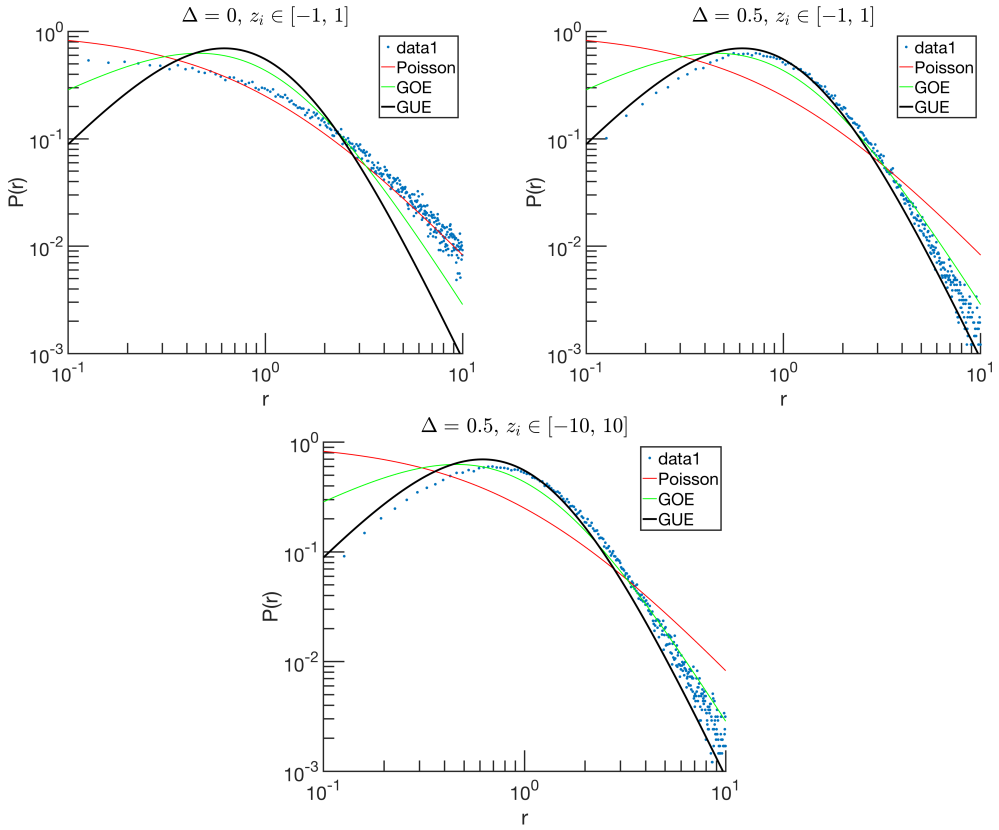

Figure 3.7: ESS generated for Anderson localization (top left), thermalization (top right), and MBL (bottom) regimes for 12 spins. For Anderson localization interactions Δ are set to zero and disorder strength z_i is a random value in the range $[-1, 1]$ (though in principle any disorder value produces AL). $\Delta = .5$ and $z_i \in [-1, 1]$ give a thermal distribution and $\Delta = .5$ and $z_i \in [-10, 10]$ give a MBL distribution.

The plots in Fig 3.7 match well with the results presented in [9]: Poisson for AL, GUE for thermalization, and nearly GUE for MBL. The fit of the data to the Poisson distribution for low ratio values in the AL regime is slightly worse than that of the paper, which may be due to them unfolding before taking ratios. Unfolding with the methods detailed in Appendix A improves the fit for low values of r, but worsens the fit for the tail end of the distribution. The slight deviation from [9] is likely due to a different unfolding method (if used) or a different method of averaging over 2000 realizations. The difference is rather slight and the AL regime is still clearly distinguishable from the thermal or MBL regime so we continued with this methodology.

Chapter 4

Results and Discussion

While EES and ESS are both insightful metrics, I worked mainly with EES to generate a phase space diagram. Because EES does not require time evolution and thus does not require exponentiation of large matrices, it was much faster to work with than ESS. With EES I was able to map out more comprehensive phase space diagrams with larger spin systems, better statistical accuracy, and for a greater variety of systems. Once I identified points of interest using EES, I could then probe those regions using ESS.

4.1 EES Results

The phase space I explored was that of the Hamiltonian of Eqn 2.9

$$H = J\sum_{i=1}^{L-1}\left[\frac{u+v}{2}\sigma_x^i\sigma_x^{i+1} + \frac{v-u}{2}\sigma_y^i\sigma_y^{i+1} - v\sigma_z^i\sigma_z^{i+1}\right] + \sum_\alpha g_\alpha \sum_{i=1}^{L} c_\alpha^i \sigma_\alpha^i \quad (4.1)$$

with varying strengths of disorder g and interactions v. I kept disorder values equal in the z and x directions and set y directional disorder to zero ($g_z = g_x \neq 0,\ g_y = 0$) following in the footsteps of [7]. Therefore varying g here means varying $g_z = g_x$ while keeping $g_y = 0$. Overall interaction strength J is set to $J = 1$ and u and v follow the relation $\sqrt{(u^2 + v^2)/2} = 1$ to normalize the energy scale of the system.

The parameter space of g and v ranged from $g = 0.1$ to 9 and $v = 0$ to 1, both in increments of 0.1. In order to most clearly represent the phase space in my plots, I decided to use a color plot showing the fit strength of the min/max ratio data to a GOE Wigner-Dyson distribution. The fit strengths are normalized according to coefficients of a linear combination of GOE and Semi-Poisson (SP) distributions. That is, the color plots show the value $\gamma/\sqrt{\beta + \gamma}$ extracted from the fit

$$f^{(fit)}(r) = \beta f^{(SP)}(r) + \gamma f^{(GOE)}(r) \tag{4.2}$$

where the coefficient values here are completely unrelated from the interpolation parameters of Section 3.2.2.

I did not include Poisson and GUE distributions in the fit because I knew that none of the statistics in my phase space regime pertained to those distributions. Since all of the studied parameter space represents an interacting system with disorder (except $v = 0$, which is noninteracting), the regions with nonzero v should obey either Wigner-Dyson statistics (for ther-

malization) or Semi-Poisson statistics (for MBL). Normally, the regions with $v = 0$ should obey Poisson statistics representing integrability since a noninteracting system with nonzero disorder exhibits AL. However, the inclusion of transverse disorder breaks the symmetries required for Poisson statistics, which we do by setting $g_z = g_x$. Keeping $g_y = 0$ prevents the breaking of additional symmetries that would change Wigner-Dyson Gaussian statistics from orthogonal to unitary as noted in [7], so GUE can also be ruled out. The good fit to SP and GOE (and lack of fit to Poisson and GUE) can be seen in Fig 4.1. Fig 4.2 shows the switch from Poisson to GOE statistics when symmetries are broken with transverse disorder. Fig 4.3 shows the switch from orthogonal to unitary symmetry when y directional disorder is added.

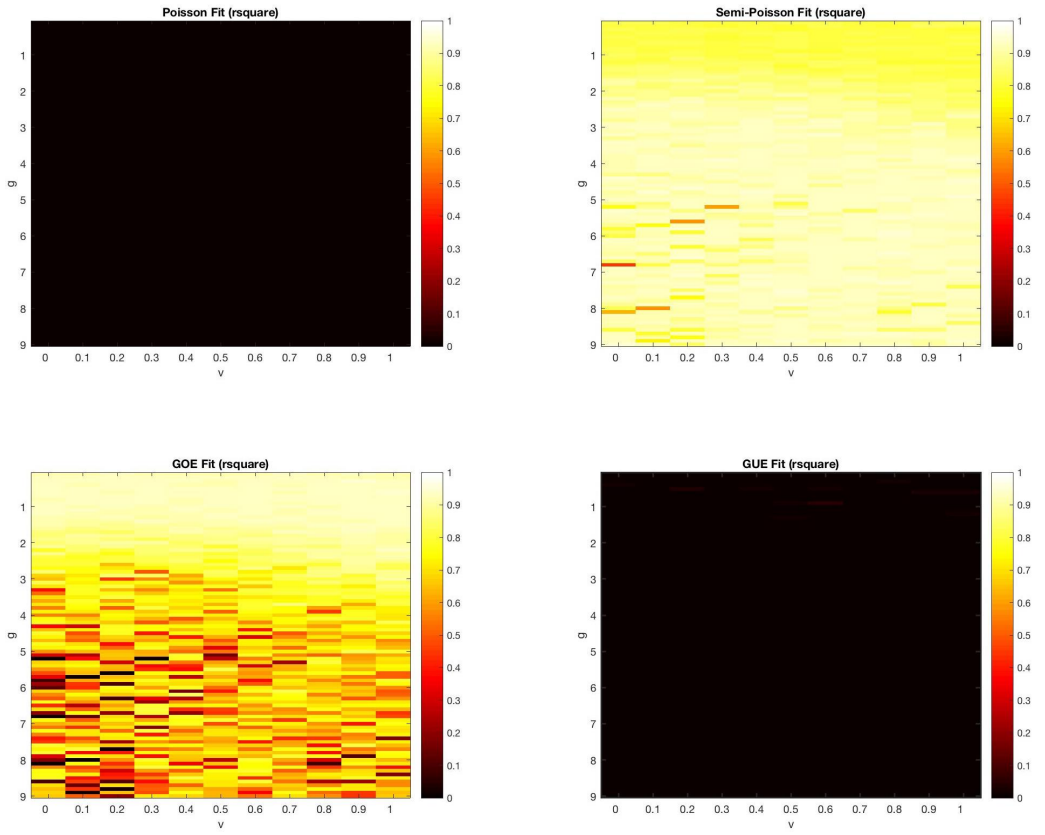

Figure 4.1: Phase space diagrams depicting the strength of data fitting to each of the four distributions. The values plotted are the R^2 values of fitting. The plots indicate a lack of correlation of the data to either Poisson or GUE, but good correlation to SP and GOE.

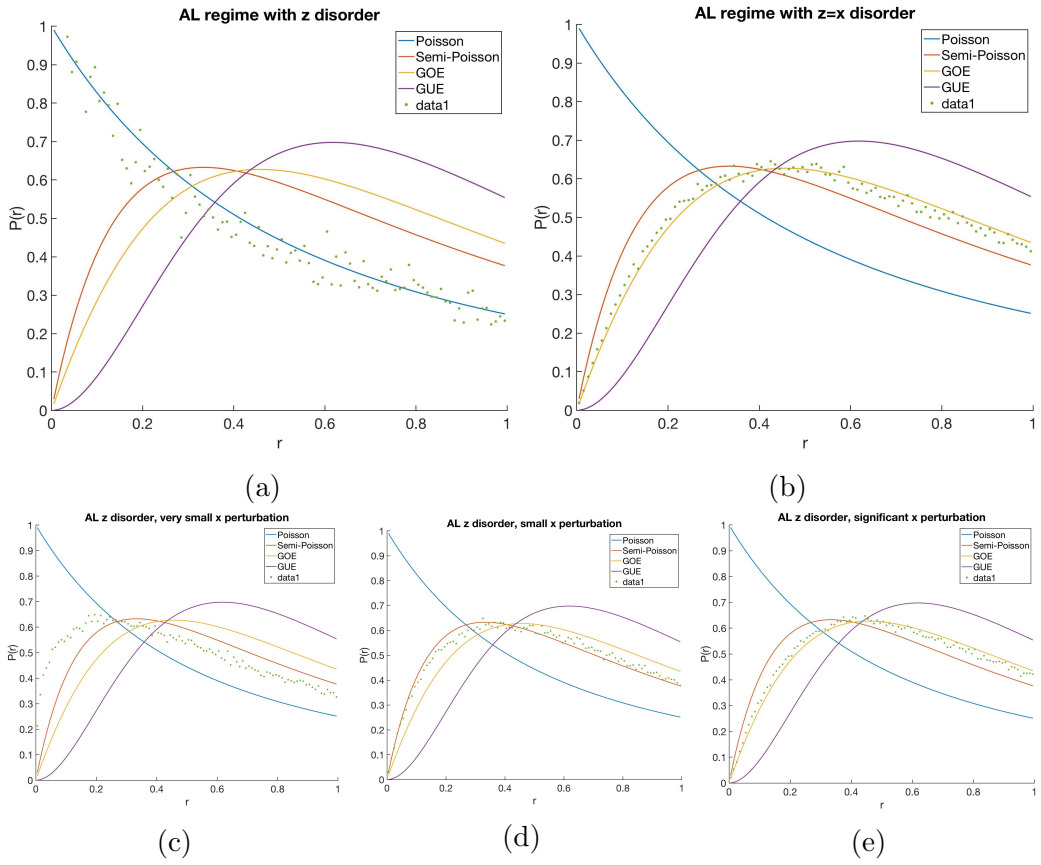

Figure 4.2: Plots showing the breaking of symmetries caused by transverse disorder in the noninteracting regime (v=0) for 12 spins with a 6-6 partition. (a) Shows spectral data following a Poisson distribution for $g_z = 0.25$. In (b) transverse disorder is added so $g_z = g_x = 0.25$. In principle, even a small uniform field in the transverse direction should break symmetries so that the data does not follow Poisson statistics. This is shown in plots (c)-(e), in which a uniform transverse field in the x direction is added to disorder $g_z = 0.25,\ g_x = g_y = 0$. The uniform field increases along the bottom three plots as (c) 0.001, (d) 0.01, (e) 0.1. Even a very small transverse perturbation prevents the data from exhibiting Poisson statistics.

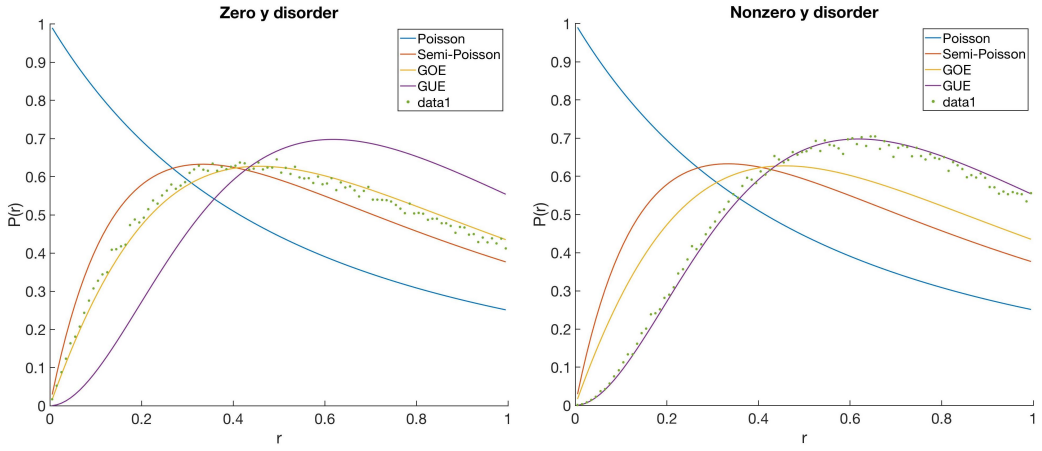

(a) (b)

Figure 4.3: Plots showing the switch from unitary to orthogonal symmetry when y directional disorder is added. The plots depict a 12 spin system with a 6-6 partition in a thermal regime: $v = 0.5$ and $g = 0.25$. (a) Shows GOE statistics for no disorder in the y direction. (b) shows GUE statistics for $g_z = g_x = g_y = 0.25$.

With two two distribtions of relevance (Semi-Poisson and GOE) determined, an example of a phase space diagram is shown in Fig 4.4. Disorder strength g varies along the y-axis and interaction strength v varies along the x-axis. The righthand side shows a colormap where bright yellow indicates a strong fit to a GOE distribution and black indicates a good fit to a SP distribution.

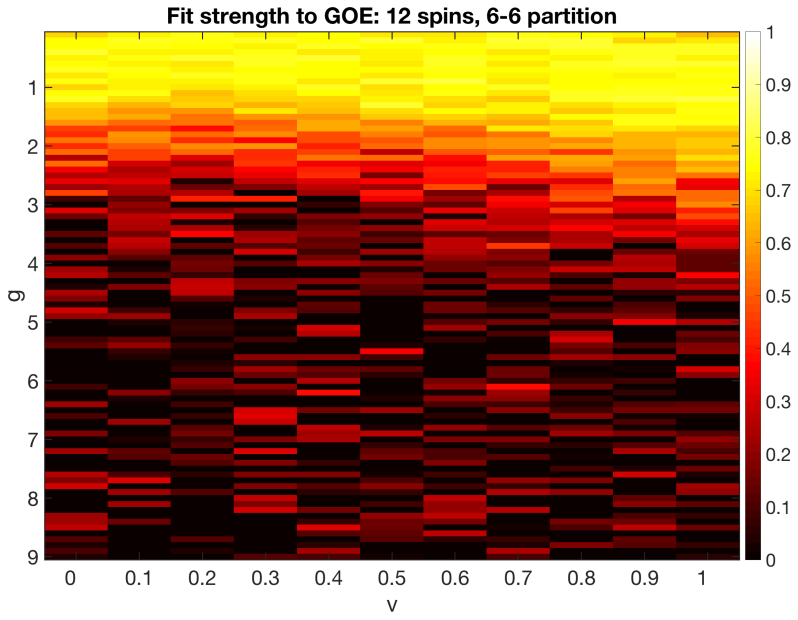

Figure 4.4: Phase space diagram depicting the strength of fit of min/max ratio data to a GOE distribution for $g_x = g_z \neq 0,\ g_y = 0$ for 12 spins with a 6-6 partition. The value plotted is a normalized coefficient of fit to the GOE distribution in a sum of Semi-Poisson and GOE distributions: $\gamma/\sqrt{\beta+\gamma}$.

Fig 4.4 depicts some broad characteristics that match expectations. Thermalization is expected for weak disorder in an interacting system and MBL is expected for strong disorder, so the bright yellow top contrasting with the dark red/black bottom is consistent with the two cases. There is a transition region between thermal and MBL where the colors switch from predominantly yellow to red. The colors around the transition region are dark yellow, orange, and light red, which indicate a distribution intermediate between GOE and SP. As interaction strength increases, stronger disorder is expected to be necessary for the system to exhibit MBL. This explains the

curvature of the transition region downward (towards higher disorder) as v increases.

Despite a clear difference between the thermal and MBL regimes in the color plot, there are still many hints of red in the MBL regime which indicate data that are intermediate between the two distributions. This may represent some degeneracies caused by reflection symmetry since the partition is down the middle (6-6). This motivated the exploration of unequal bipartitions to see if different partitions would break reflection symmetry and show less intermediate data. Another motivation was that the partition location can affect the level of entanglement present between the two subsystems. If we consider the bipartite EE of Eqn 3.6, different subsystem definitions for A and B can result in different bipartite EE values S_A. Fig 4.5 shows results for 12 spin systems with unequal partitions of 7-5 and 10-2. All partial traces for data taken are performed over the left (larger) subsystem for maximal statistical averaging.

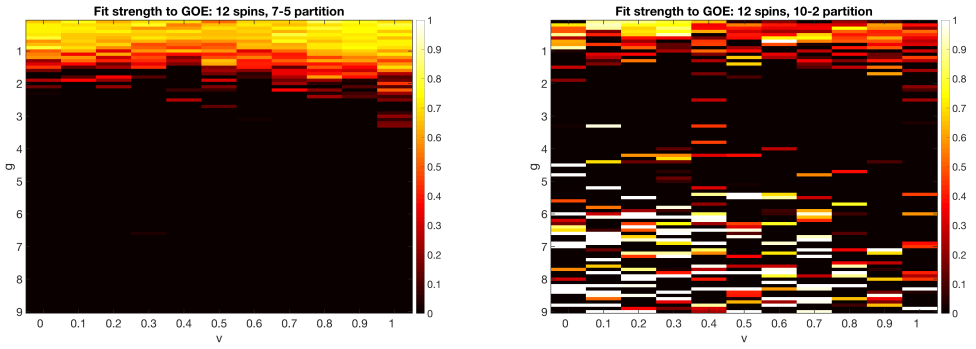

(a) (b)

Figure 4.5: Phase space diagrams for 12 spin systems with unequal partitions of (a) 7-5 and (b) 10-2. (a) shows very strong fits to GOE and SP in the thermal and MBL regimes, respectively. This indicates that breaking of reflection symmetry reduces extra degeneracies in the system. (b) shows a lot of erratic behavior in the deep thermal and MBL regimes, which may be a result of statistical inaccuracy when dealing with large differences in subsystems size.

The results in Fig 4.5 are interesting because they show the importance of the choice of bipartition location. Fig 4.5a suggests that the breaking of reflection symmetry reduces degeneracies present in a system of equal partitions, which makes the difference between thermalized and MBL regions very clear. However, Fig 4.5b suggests that we must be careful in choosing the location of the bipartition. The 10-2 partition makes the subsystem sizes heavily lopsided, which may make it hard to use statistical analysis.

Another possible parameter affecting the dynamics is the chain length, where deviations could arise from finite-size effects appearing differently in different size chains. As depicted in Fig B.4, increasing chain length can reduce the size of the region of transition from thermalization to MBL. Fig 4.6

shows results for two chains of odd length (11 and 13 spins) with 6-5 and 7-6 partitions, respectively.

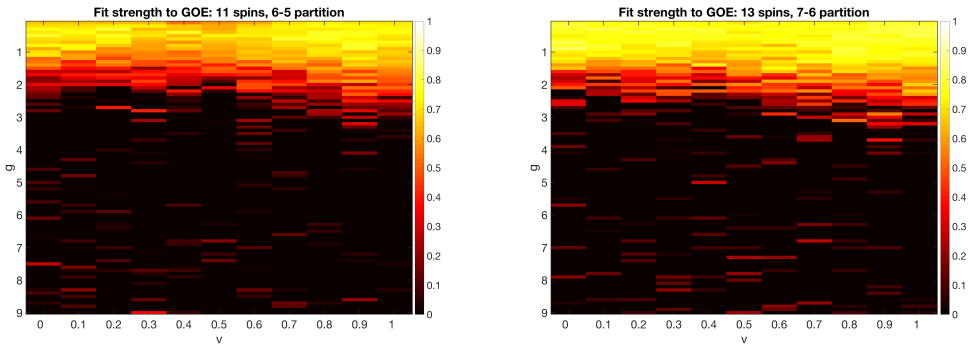

(a) (b)

Figure 4.6: (a) Phase diagram for spin chain size 11 with a 6-5 partition. (b) Phase diagram for spin chain size 13 with a 7-6 partition. Though there might be some differences in the size of the transition region, it is difficult to tell. The apparent higher degree of mixing in the $L = 11$ chain can also be a result of more statistical variation (less averaging).

The two plots in Fig 4.6 are relatively similar. They both exhibit a strong difference in distributions in regions of thermalization (GOE) and MBL (SP), especially when compared to the even partition of Fig 4.4; with an odd length chain, reflection symmetry is inherently broken for any partition. However, since the spin chain lengths are so similar, it is difficult to say whether there is a difference in the size of the transition region. Though the 13 spin system may seem to have a slightly smaller transition region, this could also be do to higher statistical fluctuation in the smaller system. Because the 11 spin system is smaller, there are fewer eigenstates over which to average. This would cause increased statistical fluctuation compared to the larger system,

which makes the distinction between GOE and SP more difficult for the fit function. Thus a seemingly larger transition region in the spin 11 system may not totally be due to the difference in system size. In any case, the difference in spin chain length is so small that it would be hard to see significant differences (see, for example Fig B.4; the transition region for $L = 11$ and $L = 13$ are very similar in size). Though it would be beneficial to explore chains of much greater length, we are limited by computational power.

Fig 4.7 shows results for 14 spins, which exhibit similar behavior to the 12 spin system. There is a high indication of degeneracy shown by red coloring for the even 7-7 partition in Fig 4.7a, but those degeneracies are heavily reduced when reflection symmetry is broken with an unequal bipartition in Fig 4.7b. Again, it is difficult to compare transition region sizes of 14 and 12 spins since the difference in spin chains sizes are very small compared to the range of lengths shown in Fig [17].

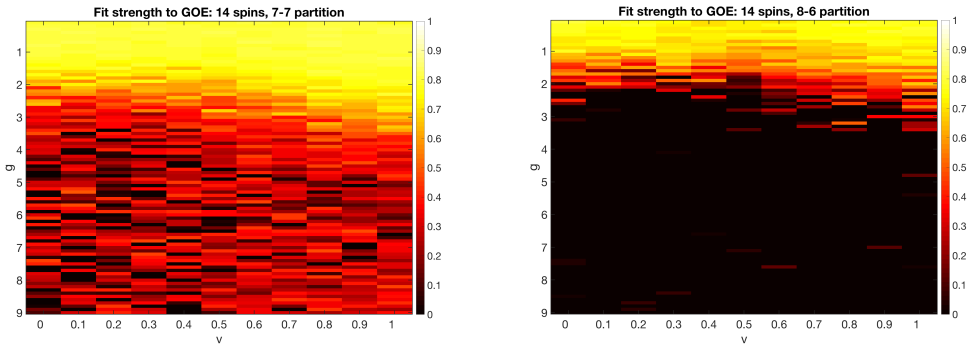

(a) (b)

Figure 4.7: Phase diagrams for 14 spin systems of partitions (a) 7-7 and (b) 8-6.

4.2 ESS Results

With phase space diagrams generated using EES, I could then probe regions of interest using ESS. ESS has the benefit of allowing us to explore dynamics at varying timescales. For example, because the FAP system can be approximated as a 1D NN coupled spin chain only at short timescales, it is of experimental interest to examine dynamics at short times. In general for quantum information processing, it is of interest to be able to retain information locally for long timescales - therefore in that context it is useful to be able to explore dynamics at long timescales.

As a basic test of ESS for our Hamiltonian, consider Fig 4.8. For disorder values of $g_z = 1,\ g_x = g_y = 0$, with no interactions the ratio data follow a Poisson distribution even at a long timescale of $t = 1000$ in units of $1/J$. As soon as interactions are turned on, the data switch to a GOE distribution indicating thermalization. Further increasing interaction strength breaks orthogonal symmetry and changes the distribution to GUE statistics, which may be an indication of breaking time-reversal symmetry. Though not depicted, the data remain GUE as interaction strength continues to increase. These results are consistent with the expectation of AL behavior for nonzero disorder and no interactions, and a switch to thermalization as soon as interactions are turned on.

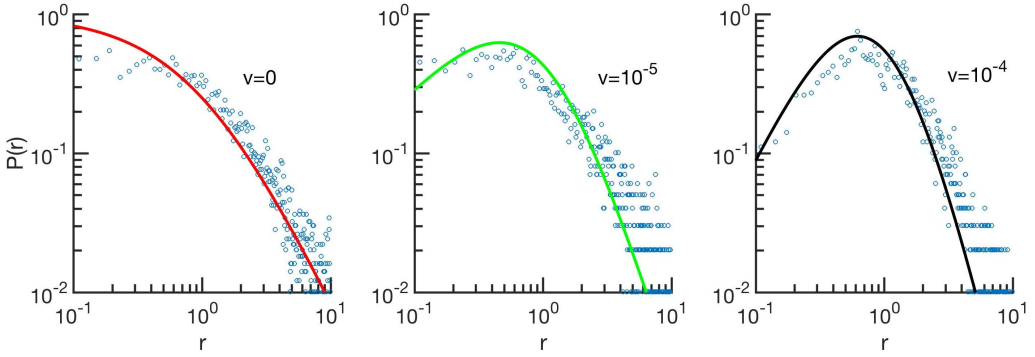

Figure 4.8: ESS ratio plots for a 12 spin 6-6 bipartition system with $g_z = 1$, $g_x = g_y = 0$, varying interaction strength v, and $t = 1000$ time steps in units of $1/J$. Interaction strength (as depicted) increases from left to right as $v = 0$, $v = 10^{-5}$, $v = 10^{-4}$. The ratio data transition from Poisson to GOE to GUE statistics, and remain GUE for higher interaction strengths. N.B. these plots were generated without keeping $u^2 + v^2$ constant, so the energy scale is not constant; instead, $u = 1$.

Instead of varying interaction strength, we can also vary disorder strength to test expectations. Figs 4.9 and 4.10 depict results for systems with interaction strength $v = 0.1$ and varying disorder strengths. In Fig 4.9 we can see that in this interacting system the ratio data exhibit GUE statistics for any value of g_z (and $g_x = g_y = 0$) that is sufficiently low for $t = 1000$. This is consistent with the expectation of thermalization for an interacting system with low disorder.

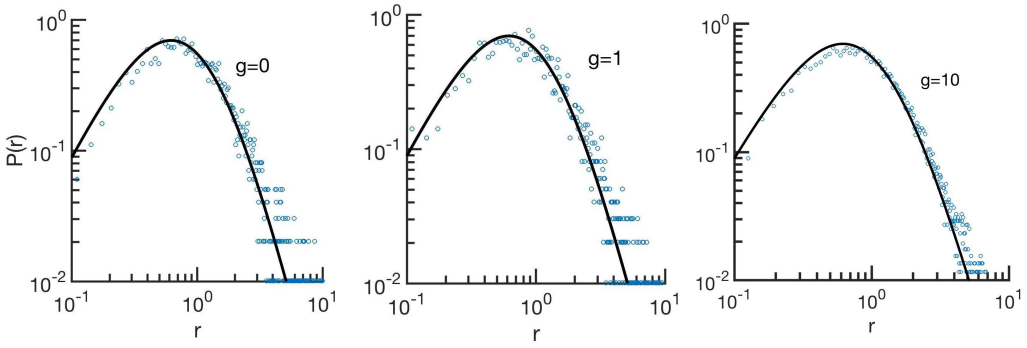

Figure 4.9: ESS ratio distributions for systems with interaction strength $v = 0.1$, varying disorder strengths, and $t = 1000$. Disorder strength (as depicted) increases from left to right as $g = 0$, $g = 1$, $g = 10$. The ratio data remain GUE even for strong disorder, which does not capture a possible transition to MBL. N.B. these plots were generated with $u = 1$.

We would expect that as disorder strength increases, eventually the system would exhibit MBL. The rightmost plot in Fig 4.9, for example, features disorder that should be strong enough for MBL. However, disorder strength is not the only parameter that can affect the dynamics that the distributions reflect. Another reason that ESS data for higher disorder may continue to exhibit GUE statistics is that we are examining the system at long times of $t = 1000$. Viewing the system at shorter times could change the distributions as entanglement is not given as much time to spread throughout the system. Shorter timescales are also of interest to this system because the 1D NN coupling approximation for FAP is valid only over short timescales. Fig 4.10 depicts an increase of disorder g from 0 to 10 for a shorter timescale of $t = 20$. Compared to Fig 4.9, already at $g_z = 1$ the data show a departure

from GUE statistics that was not present for long timescales. As disorder increases in Fig 4.10, there is a clear transition from GUE to Poisson statistics. This shows that the data exhibit different behavior if we examine the system at shorter timescales, thereby not allowing entanglement to spread over the entire system.

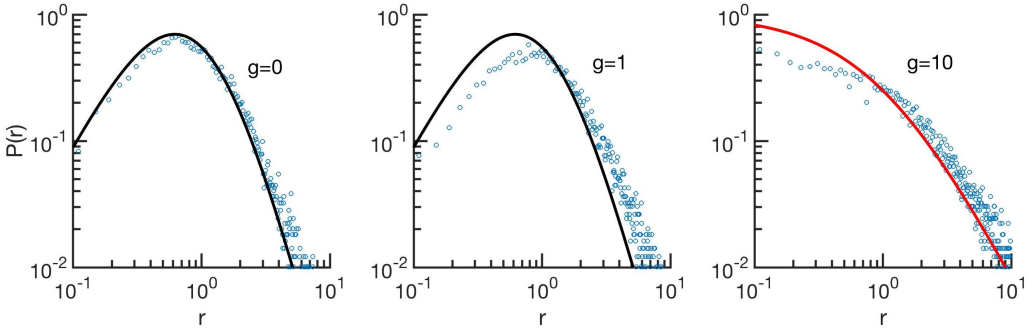

Figure 4.10: ESS ratio distributions for systems with interaction strength $v = 0.1$, varying disorder strengths, and $t = 20$. Disorder strength (as depicted) increases from left to right as $g = 0$, $g = 1$, $g = 10$. The ratio data switches clearly to a Poisson distribution, which indicates a MBL phase transition. Studying the system at short times prohibits entanglement from spreading through the system, which allows us to see Poisson statistics for MBL. N.B. these plots were generated with $u = 1$.

Keeping these ideas in mind, we used ESS to explore some regions of the EES 12 spin phase space diagram (Fig 4.4). Timescales are kept short ($t = 20$) in consideration of the short times over which the FAP crystal can be approximated as a 1D NN coupled spin chain system. A noticeable difference from the ESS discussion above is that disorder strength g now refers to the same values as the EES, so in general $g_z = g_x \neq 0$, $g_y = 0$. Results are shown in Fig 4.11.

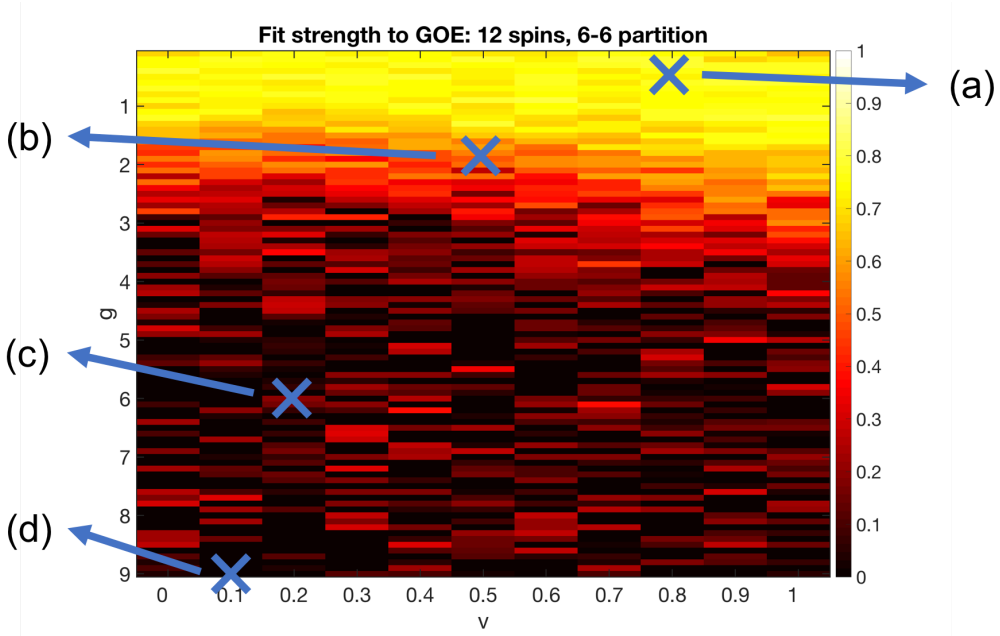
Fit strength to GOE: 12 spins, 6-6 partition
(a)
(b)
(c)
(d)
g
v
1
2
3
4
5
6
7
8
9
0
0.1
0.2
0.3
0.4
0.5
0.6
0.7
0.8
0.9
1

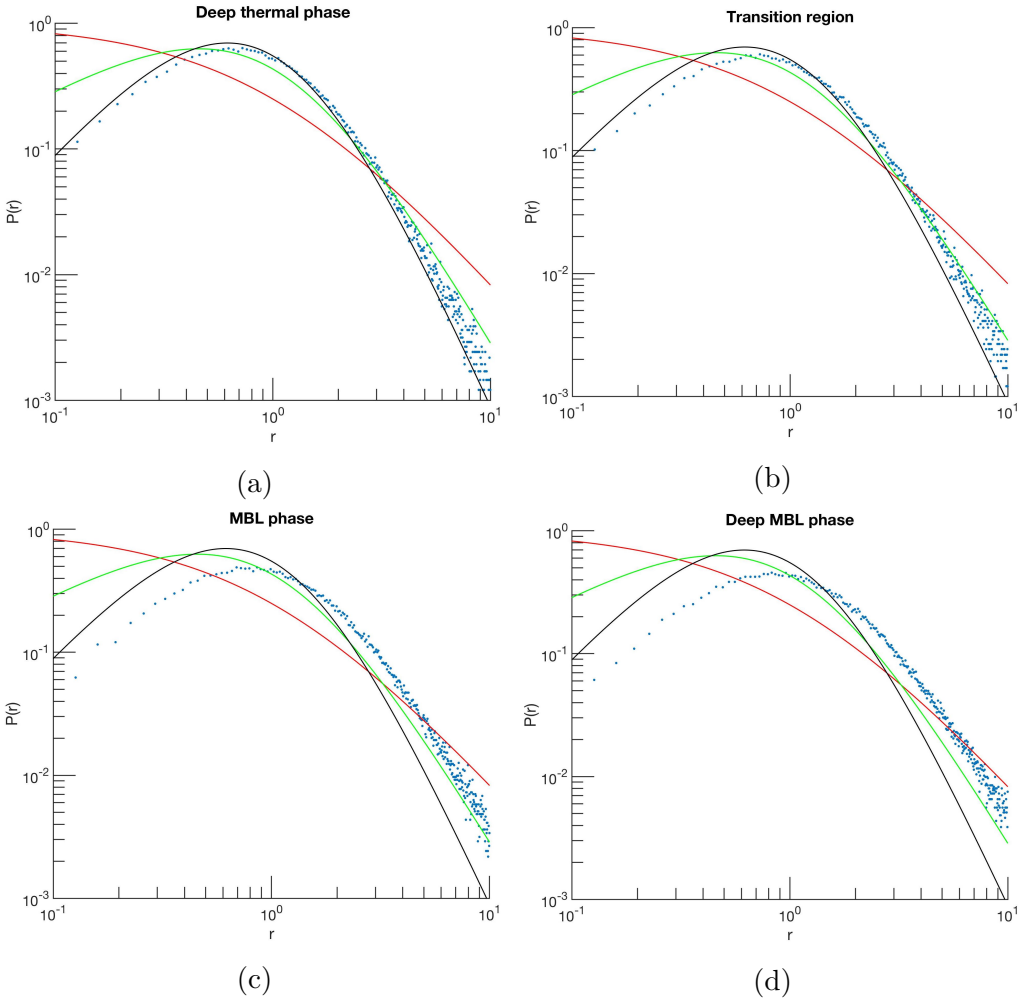

Figure 4.11: ESS ratio distributions for several points on the EES phase space diagram of Fig 4.4. The points chosen from Fig 4.4 are shown in the top plot. The g and v values explored are (a) $g = 0.5$, $v = 0.8$ for a point in the thermal phase, (b) $g = 2$, $v = 0.5$ for a point in the transition region, (c) $g = 6$, $v = 0.2$ for a point in the MBL phase, and (d) $g = 9$, $v = 0.1$ for a point deep in the MBL phase. All data are taken at $t = 20$ time steps in units of $1/J$ with 2000 realizations (now over both random initial state and disorder for each realization).

The ESS data closely follow GUE statistics for the deep thermal phase

and show a slight departure in the transition region, as expected. The data continue to depart from GUE statistics in deeper MBL regions, but there is no transition to Poisson statistics for the disorder values shown in Fig 4.11. The relative values of interaction and disorder strengths are such that the data would reflect MBL behavior according to Fig 4.10, but it is not the case for Fig 4.11. We can reconcile this by noting two differences: firstly, for the data in Fig 4.11, there is z and x directional disorder, which may be causing symmetry breaking that prevents a switch to Poisson. Secondly, for the data in Fig 4.10, $u^2 + v^2$ is not the same value as in Fig 4.11. Therefore the lack of Poisson statistics in the parameter space in Fig 4.11 compared to Fig 4.10 may be caused by a different energy scale normalization. To test what disorder strength would produce Poisson statistics for the normalized energy scale of the data in Fig 4.11, ESS plots were generated for higher disorder values. The results are shown in Fig 4.12 and Fig 4.13. Interestingly, the addition of x directional disorder causes the transition to Poisson statistics to take longer than if there is only z directional disorder. Though ESS does not seem to be as sensitive to symmetries as EES, the slower transition to Poisson statistics for Fig 4.12 implies that ESS data is affected by symmetry breaking as well.

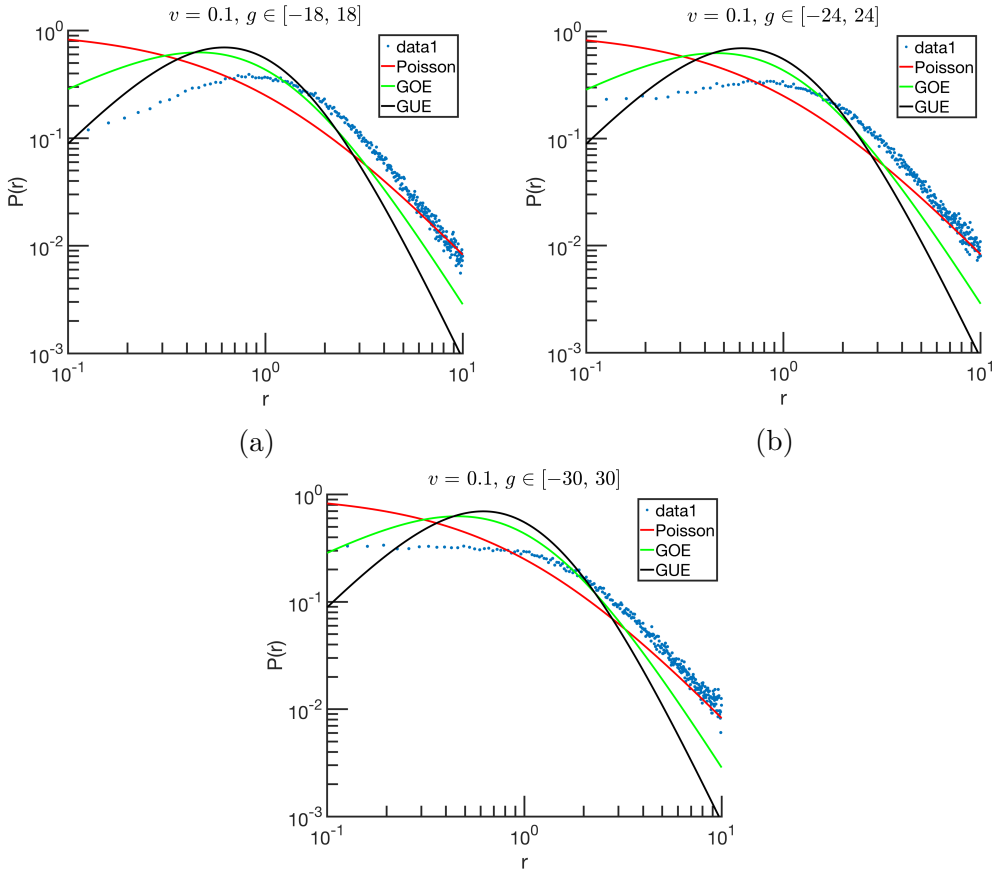

Figure 4.12: Data generated for interaction strength $v = 0.1$ and disorder varying from (a) $g_z = g_x = 18$, (b) $g_z = g_x = 24$, (c) $g_z = g_x = 30$. All data are taken at $t = 20$ time steps in units of $1/J$ with 2000 realizations (over both random initial state and disorder for each realization). The energy scale is normalized to $u^2 + v^2$=2. The data slowly moves towards a Poisson distribution as disorder is increased, but it takes very strong disorder to see hints of Poisson statistics. This suggests that the difference in energy scale and presence of symmetry breaking cause a substantial difference from the data in Fig 4.10.

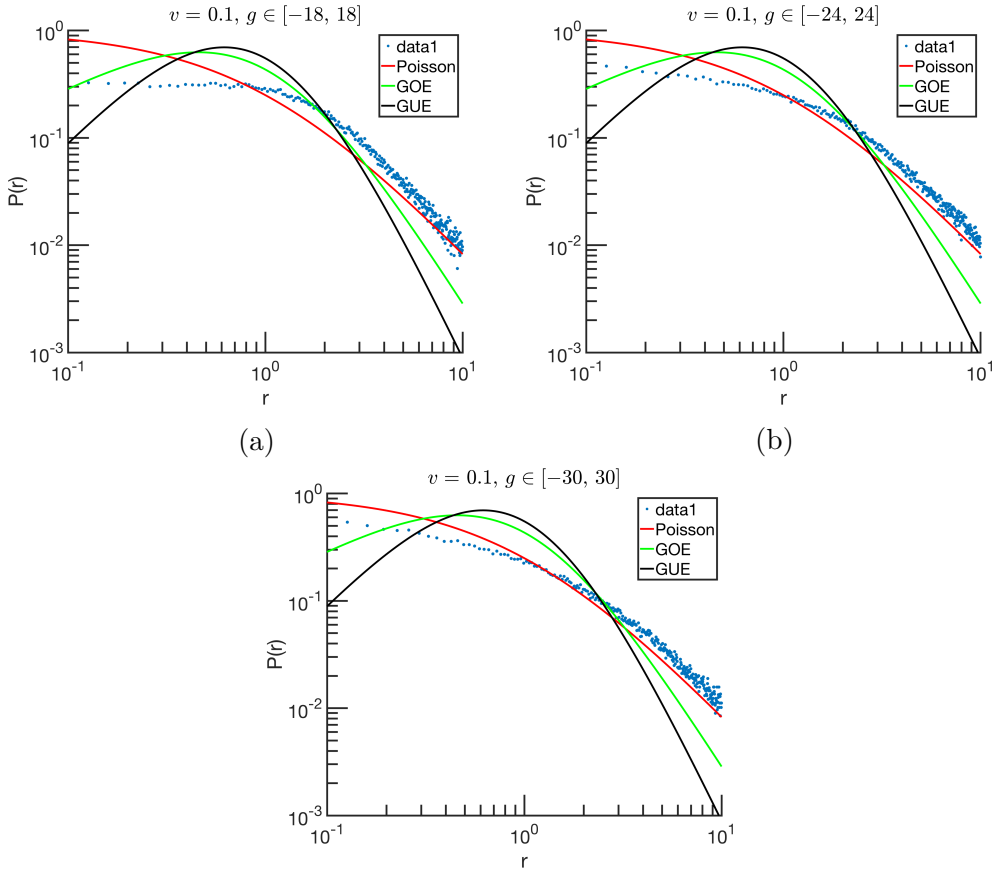

Figure 4.13: Data generated for interaction strength $v = 0.1$ and disorder varying from (a) $g_z = 18$, (b) $g_z = 24$, (c) $g_z = 30$. All data are taken at $t = 20$ time steps in units of $1/J$ with 2000 realizations (over both random initial state and disorder for each realization). The energy scale is normalized to $u^2 + v^2$=2. The data approaches a Poisson distribution more rapidly than when there is also x directional disorder, but still much more slowly than the data in Fig 4.10. This data suggests that the energy scale makes a rather significant difference.

Conclusions

The Eigenstate Entanglement Spectrum (EES) and Entanglement Spectrum Statistics (ESS) together provide very useful ways to explore complex dynamics in quantum systems. Using the EES, I was able to map out phase space diagrams of systems of varying size and partitions and with ESS I could probe the time-dependence of some dynamics. Therefore the two metrics provide considerable insight into using quantum statistical mechanics to explore many-body eigenstates, interactions and disorder, entanglement, and some time-dependent dynamics.

However, there are several shortcomings of the two metrics. Both metrics are not directly applicable to the experimental NMR setup because spectral metrics cannot be measured directly. For the EES, the results follow proposed distributions only if the dynamics are sufficiently complicated; for example, systems without disorder did not produce data that followed a distribution. For ESS, the exponentiation of matrices in the time evolution makes simulations significantly longer than those for the EES. It was therefore more time consuming with ESS to gather enough data to average over to reduce

statistical fluctuations.

Motivated by these shortcomings, there are many future directions to take to further explore the dynamics of the fluorapatite (FAP) NMR engineered Hamiltonian. Concerning the experimental applicability of spectral results, a possible solution is to correlate these results with measurable metrics (such as OTOCs studied in [2]). For dynamics not complex enough to be reflected in the EES, one could use other entanglement metrics such as EE or the Schmidt gap to explore varying interaction strengths. Mainly for ESS (but in general for any time-dependent metric), looking for ways to optimize time evolution calculations can lead to faster data acquisition. Also, it is of interest to explore longer-time dynamics of this spin chain. Another point of interest is the transition region between thermalization and many-body localization, i.e. the many-body mobility edge. We can further probe this region by averaging over smaller regions of eigenstates using the EES, but it would also be of interest to explore other methods to study this dynamical transition.

Appendices

Appendix A

Unfolding Procedure

When taking the spacings of eigenvalues of the full level density spectrum, one needs to take into account the overall level dependence of local level fluctuations. If the level density is not uniform (which is the case in systems we study, c.f. Fig A.1), then local averages of level spacings vary across the eigenvalue levels. This complicates the use of RMT ensembles to study level statistics because RMT ensembles have traditionally been used to explain energy level correlations that are independent of mean level spacing [18]. We therefore want to use an unfolding procedure to average over level density variations. The unfolded spectral values should be both locally and globally normalized so that the mean level spacing is constant everywhere.

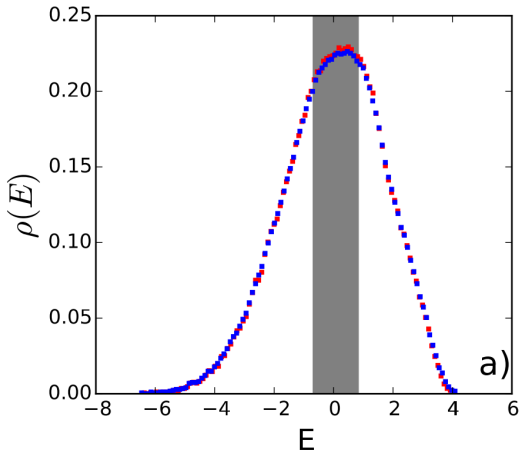

Figure A.1: Energy density distribution of a Heisenberg spin chain with x, y, and z directional disorder taken from [7]. The shaded region corresponds to the middle third of the energy spectrum. The energy density varies significantly over the energy spectrum, especially in regions outside the middle third eigenenergies.

The usual unfolding procedure is to compute the cumulative spectral function of the original spectral values. It takes into account local changes in eigenvalue densities by including the number of eigenvalue levels at or below the target eigenvalue E. Thus when the local mean level density $\rho(E)$ is known, the unfolded variable can be defined as

$$\lambda(E) = \int_{-\infty}^{E} \rho(E')dE' \tag{A.1}$$

for a continuous spectrum. For a discrete spectrum, the unfolded values $\lambda_i = \lambda(E_i)$ constitute the unfolded spectrum which can then be used to generate distributions of spacings $s_i = \lambda_{i+1} - \lambda_i$. The unfolded variable is dimensionless and has mean level spacing unity everywhere such that $\langle 1 \rangle =$

$\langle s \rangle = 1$, so its spectrum can be compared to relevant RMT ensembles.

The spacing between adjacent unfolded levels can also be expressed in an approximated way that is potentially easier to implement numerically (as is used in [19]). The spacings can be Taylor expanded as

$$s_i = \lambda_{i+1} - \lambda_i = (E_{i+1} - E_i)\frac{d\lambda_i}{dE_i} + \text{h.o.t} = \frac{(E_{i+1} - E_i)}{D_i} + \text{h.o.t} \qquad \text{(A.2)}$$

where $D_i = 1/\rho(E_i)$ is the mean local level spacing near E_i and h.o.t stands for higher order terms. When the level density is varying slowly enough (which is true especially near the middle of the energy spectrum), the higher order terms can be neglected [18]. This leaves us with a direct relationship between the original and unfolded spectra

$$s_i = \frac{(E_{i+1} - E_i)}{D_i}. \qquad \text{(A.3)}$$

As mentioned in Section 3.2.1, the ratios of Eqn 3.8 may not require unfolding if the level density varies slowly. To see why, consider the calculation of ratios using Eqn A.3 - if adjacent density values are approximately equal, they have little effect on the ratio value. The ratio of consecutive unfolded spacings using Eqn A.3 is

$$r_i = \frac{s_{i-1}}{s_i} = \frac{E_i - E_{i-1}}{E_{i+1} - E_i}\frac{D_i}{D_{i-1}}. \qquad \text{(A.4)}$$

If the level density varies slowly, then $d\lambda/dE$ does not vary much between

adjacent sites. This results in a ratio of adjacent local energy spacings $D_i/D_{i-1} \approx 1$, so Eqn A.4 becomes approximately equivalent to Eqn 3.8. Thus the above definition of ratios may not require unfolding as long as the energy density varies sufficiently slowly. For more detail about numerical methodology of unfolding with a discrete spectrum, see [19] or Appendix C.

Appendix B

Many-Body Dynamics

One of the central purposes of this study is to characterize the entanglement dynamics of our system of interest. There are two main catagories of dynamics that we are interested in: *thermalization* and *localization*. Thermalization refers to the ergodic spreading of entanglement over the entire system; localization describes the local retention of entanglement to a small group of particles. The subsequent explanations closely follow ideas presented in [3].

B.1 Thermalization

In broad terms, thermalization describes the long-time spreading of local entanglement over the entire system, which results in a system that can be described accurately using equilibrium quantum statistical mechanics. Quantum thermalization and quantum statistical mechanics have been studied ex-

tensively over the past century [6], but most studies have explored the properties of a quantum system in contact with an external reservoir. However, closed systems (systems which are not in contact with an external system) have also been shown to thermalize. This can happen when the closed system acts as its own reservoir. Fig 1.2 includes conceptual diagrams helpful for picturing the quantum system.

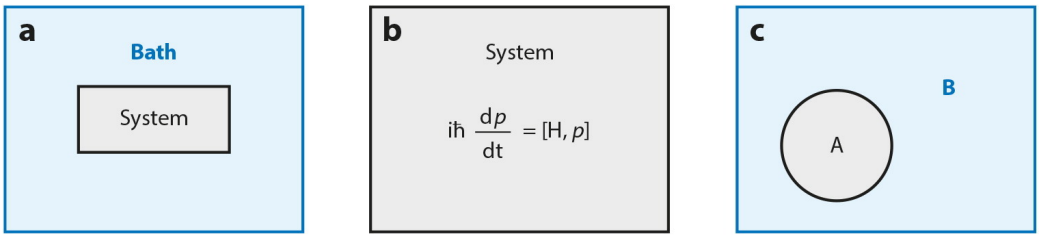

Figure B.1: Taken from [3]. (a) Traditional treatment of quantum systems in quantum statistical mechanics with a system in contact with a reservoir (or bath). (b) In our systems we are concerned with unitary time evolution of the system, i.e. $|\psi(t)\rangle = U|\psi_0\rangle = e^{-iHt}|\psi_0\rangle$. (c) For a closed quantum system, we can define a subsystem A that is in contact with the rest of the system B, such that B acts as a reservoir for A.

Consider a system that is partitioned into subsystems A and B. In order for B to act as a bath, subsystem A must contain a small number of degrees of freedom compared to the rest of the system B so that the coupling of A to the rest of the system acts like coupling to a reservoir. Then the long-time steady states of the subsystems can obey traditional quantum thermodynamic and quantum statistical mechanic properties of equilibrium systems. Such a system is said to be thermalized. Though it is convenient to picture the segregation of subsystem A from the rest of the system to be spatial, it

need not be the case. Subsystem A can be separated in momentum space or by a set of degrees of freedom that are far away in real space.

Now to make the example more concrete, let us define some initial state $\rho(t = 0)$ and look at its long-time behavior in a system that is partitioned in real space into subsystems A and B. If this initial state does indeed thermalize after some time t to a temperature T, then the system has an equilibrium expectation value of the total energy $\langle H \rangle_T$ and is described by the Boltzmann probability operator $\rho^{(eq)}(t) = e^{-\beta H}/Z$ where $\beta = 1/k_B T$ and $Z = \mathrm{Tr} \exp(-\beta H)$. From the total density matrix we obtain the reduced density matrix $\rho_A(t)$ of subsystem A by taking the partial trace over all the degrees of freedom in B: $\rho_A(t) = \mathrm{Tr}_B \, \rho(t)$. Thus when the total system is at thermal equilibrium, the reduced density matrix becomes $\rho_A^{(eq)}(t) = \mathrm{Tr}_B \, \rho^{(eq)}(t)$. $\rho_A^{(eq)}(t)$ then takes the form $\rho_A^{(eq)} = \sum_i e^{-\beta \epsilon_i} \, |A_i\rangle \, \langle A_i|$, where we can define the so-called "entanglement Hamiltonian" $H_{ent}^{(eq)} = -\ln \rho_A^{(eq)}$ such that $\rho_A^{(eq)}(t) = e^{-\beta H_{(ent)}}/Z$ (at least at high temperatures). In order for thermalization to be of particular interest in a thermalizing system, initial states far from equilibrium should eventually thermalize. Indeed the conventional theory in equilibrium statistical mechanics is that, for a system that thermalizes, all out-of-equilibrium initial states at a given energy will thermalize to equilibrium at the corresponding temperature in the limit of infinite time.

B.1.1 Eigenstate Thermalization Hypothesis

If a thermalizing system does indeed thermalize for every initial state, then we can consider the thermalization of a system prepared in a pure state that is one of the many-body eigenstates of H such that $H|\psi_n\rangle = E_n|\psi_n\rangle$. Eigenstates are constants of motion, so the time evolution is trivial: $\rho(t) = \rho(0)$. Since the thermalization of all initial states requires that $\rho(t)$ must thermalize, this implies that all many-body eigenstates of H are thermal. This statement is the Eigenstate Thermalization Hypothesis (ETH). To define the ETH more precisely, we note that the energy E_n of an eigenstate is the thermal equilibrium energy at temperature T_n, so $E_n = \langle H \rangle_{T_n}$. If the full system is in this eigenstate, then $\rho = |\psi_n\rangle\langle\psi_n|$ so $\rho_A = \mathrm{Tr}_B |\psi_n\rangle\langle\psi_n|$. The ETH requires that in the thermodynamic limit, the subsystem is at thermal equilibrium such that $\rho_A(t) = \rho_A^{(eq)}(t)$.

Another way to state the ETH is to consider some operator $\hat{O}$, of which the matrix elements can be expressed in terms of the basis of eigenstates of H as

$$\hat{O}_{ij} = \langle\psi_i|\hat{O}|\psi_j\rangle\,. \tag{B.1}$$

Even if the system is prepared in a state in which the expectation value of $\hat{O}$, $\left\langle \hat{O} \right\rangle$, is far from its value predicted by the microcanonical ensemble, if the system obeys the ETH then eventually $\left\langle \hat{O} \right\rangle$ will evolve to its value predicted by the microcanonical ensemble. This is characterized by two behaviors of matrix elements: the difference between diagonal elements of $\hat{O}$, $\hat{O}_{i+1,i+1} -$

$\hat{O}_{i,i}$, becoming exponentially small compared to the system size and the off-diagonal elements $\hat{O}_{ij}$ being much smaller than the diagonal elements. This happens because out-of-equilibrium states have off-diagonal terms that, when written in the eigenenergy basis, represent local coherences between different eigenenergies. Quantum thermalization requires that these local coherences vanish at long times, so the off-diagonal elements must vanish as well.

B.2 Localization

Of particular interest to quantum information are classes of systems which fail to quantum thermalize and thus fail to obey the ETH. One such class are localized systems in which local correlations do not spread beyond single-particles or many-particle groups over reasonable timescales. Thus the entanglement is localized to small regions. Within localization, there are two main groupings that we are concerned with: Anderson (single-particle) localization (AL) and many-body localization (MBL). In one dimension, AL occurs in noninteracting systems with any nonzero disorder, while MBL occurs in interacting systems with sufficiently strong disorder.

The subsequent discussion of localization incorporates a phenomenology in which localization is described in terms of localized two-state pseudospins following the work of [3, 4]. To be precise, let us define the system as a chain of N spin-1/2 particles. Typically in the thermal regime, we describe this system in terms of each physical particle at site i, labeled by Pauli operators

$\vec{\sigma}_i$. Here we call these spins physical bits, or "p-bits." However, let us now consider the case where all the many-body eigenstates of the system are localized. We can then define another set of localized Pauli operators $\vec{\tau}_i$ via unitary transformation of $\vec{\sigma}_i$. These new Pauli operators $\vec{\tau}_i$ describe a system of localized pseudospins, or "l-bits," such that the Hamiltonian written in terms of $\vec{\tau}$ takes the form

$$H = E_0 + \sum_i \tau_z^i + \sum_{ij} J_{ij}\tau_z^i\tau_z^j + \sum_{n=1}^{\infty}\sum_{i,j,\{k\}} K^{(n)}_{i\{k\}j}\tau_z^i\tau_z^{k_1}...\tau_z^{k_n}\tau_z^j \qquad \text{(B.2)}$$

where E_0 is some constant energy offset that has no relevance to the system's dynamics, the sums are restricted so that each interaction term is only counted once, and the $K^{(n)}$ terms represent $(n+2)$ interactions.

Note that unitary operations do not change eigenvalues so all τ_z^i commute with each other and with H. Thus all eigenstates of H are eigenstates of all τ_z^i. The τ_z^i are then constants of motion of the system, which act as localized conserved "charges." Since the l-bits are localized, when written in terms of p-bits they are represented by a sum of products of p-bits on nearby sites. The terms have weights that fall off exponentially to the farthest p-bit involved in the operator product. The rate of exponential drop off is determined by the localization length ξ, which depends on the disorder strength and on the energy. The l-bits are thus "dressed" versions of p-bits, with a "dressing" that falls of exponentially in real space (see Fig B.2). Using this phenomenological construction, we can explore the dynamics of AL and

fully many-body localized systems.

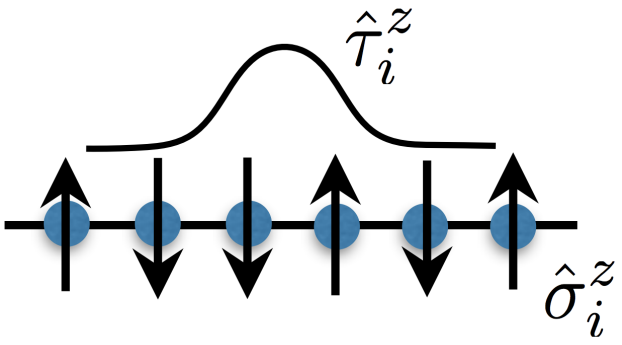

Figure B.2: A representation of dressed bits taken from [20]. The σ_i^z represent physical p-bits, while the τ_i^z represent localized l-bits.

B.2.1 Anderson Localization

Anderson localization, named after the physicist P.W. Anderson who predicted its existence in electron spin lattices, describes the exponential localization of eigenstates of the Hamiltonian in the presence of disorder. Anderson speculated that certain closed systems with random fields may fail to thermalize by solving for the propagation of a single particle in a random potential [5]. Anderson's model is known as the hopping potential, which is detailed in [21].

In 1D systems such as those of interest in this thesis, AL occurs for noninteracting systems with disorder; for example, a system of noninteracting fermions in the presence of random local magnetic fields. In this system, the

eigenstates are all exponentially localized with wavefunctions of the form

$$\psi_\alpha(\vec{r}) \sim e^{-(\vec{r}-\vec{R_\alpha})/\xi} \tag{B.3}$$

where ξ is the localization length. The state α remains localized near the position R_α at which it was initially introduced. In such a system, since there is no transport we can describe it using a set of localized conserved "charges," which we denote by τ_z^i following the above phenomenology. The lack of interactions between p-bits thus results in a lack of interactions between l-bits (in one dimension), so the dynamics do not generate any entanglement between l-bits. This explains the characteristic growth of entanglement entropy (EE) in an AL system (rapid saturation after a brief initial growth). While entanglement can spread rapidly among nearby p-bits within the localization length ξ, the lack of interaction between l-bits prevents entanglement from spreading beyond the localization length. Thus there is no transport along the chain even at infinite timescales.

If we consider an initial condition in which there is a single spin up on site i and all other spins are down, we can consider whether there is memory of that initial condition at long times. In the AL regime, since there is a localized single-particle state with weight at site i, there is a nonzero probability that the site i will hold an up spin even at infinite time. Thus memory of the initial conditions are preserved locally for infinite time, which constitutes a failure of quantum thermalization.

B.2.2 Full Many-Body Localization

If the spins are interacting, the system can still be localized for long times in the presence of strong enough disorder. When the disorder is sufficiently strong compared to interaction strengths, level splittings between sites are typically much larger than interactions. Therefore the states on different sites are only weakly hybridized, which over reasonable timescales leads to a lack of spin and energy transport required for thermalization. In such a localized interacting system, when all the many-body eigenstates of the system are localized, the system is said to be fully many-body localized (FMBL).

In a FMBL system, we can use Eqn B.2 to understand quantum dynamics in terms of l-bits. The dynamics of the l-bits are in a certain sense fairly simple: their z components are frozen, while their transverse xy components precess about the z axes of their Bloch spheres, as depicted in Fig B.3. The precession rate depends on the states of all the other τ_z^i, due to the interactions between l-bits. As a result, the xy components of each l-bit become entangled with the z components of all the other l-bits, resulting in dephasing and decoherence. However, since all the τ_z^i are conserved, there is no dissipation. Thus dephasing can be reversed by spin echo procedures, which in principle indicates that MBL systems can be used to store and retrieve quantum information [22].

Figure B.3: An illustration of the dynamical behavior of the l-bits taken from [3]. The l-bits are a set of pseudospins whose z component does not change but that precess about the z axis at a rate determined by the effective interactions with all other l-bits.

We can also use the structure of Eqn B.3 to understand the long-time logarithmic spreading of entanglement in FMBL systems. It is instructive to first consider what happens in a thermalized system and then contrast that with FMBL systems. In thermalized systems, the interaction of spins (p-bits) A and B generates entanglement between spins A and B. The subsequent interaction of spins B and C causes C to get entangled not only with B, but also with A (as long as A and B are not maximally entangled). As a result, entanglement spreads ballistically. In a FMBL system, this ballistic spreading is absent because l-bits can get entangled only through direct interaction. The interaction between two l-bits B and C depends only on their τ_z values, and since τ_z is a constant of motion, the τ_z value of l-bit B is unaffected by its interaction with l-bit A. In other words, l-bits become entangled only through direct interaction because the l-bit Hamiltonian (Eqn B.2) has no dissipation.

More quantitatively, we can define the effective interaction between l-bits

i and j as

$$J_{ij}^{eff} = J_{ij} + \sum_{n=1}^{\infty} \sum_{\{k\}} K_{i\{k\}j}^{(n)} \tau_z^{k_1} ... \tau_z^{k_n}. \tag{B.4}$$

In the localized phase it is expected that this interaction falls off with distance r between the two l-bits as $J^{eff} \sim J_0 e^{-r/\xi}$. Since the interaction J^{eff} has an influence on the phase of a precessing l-bit which becomes significant once $J^{eff} t \sim 1$ (assuming $\hbar = 1$), the interaction will entangle them after time $t \geq 1/J^{eff}$. Therefore, at time t the system's dynamics produce entanglement between all l-bits within a distance $r \sim \xi \ln(J_0 t)$ of each other. This results in logarithmic growth of entanglement over long times.

B.2.3 Many-Body Mobility Edge

The l-bit phenomenology introduced above works for systems that are FMBL, but it is not clear whether an analogous construction exists for systems that are not FMBL. In general for a spin-1/2 chain with fixed interaction strength, as the disorder strength varies from very weak to very strong, there is a quantum phase transition in which all the eigenstates switch from obeying the ETH to becoming many-body localized. However, the transition is dynamic, which means that there is some intermediate region in which not all the eigenstates are either thermalized or MBL (at least for finite size systems). Such a system with a mixture of thermalized and localized eigenstates is said to have a many-body mobility edge (MBME), which serves as a border between the thermalized and localized eigenstates of an interacting system.

The usual behavior of a system with a MBME is that all eigenstates with energy density below the mobility edge are MBL, while all eigenstates with energy density above the mobility edge obey the ETH. Fig B.4 suggests that the transition region may be a finite-size effect where the transition region does not exist for an infinite size chain.

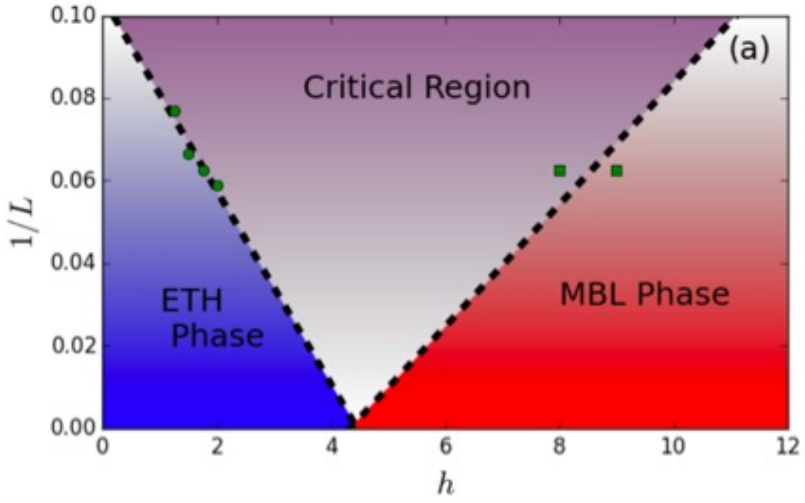

Figure B.4: Phase space diagram for $H = J\sum_i \vec{S}^i \cdot \vec{S}^{i+1} + h\sum_i (c_x^i S_x^i + c_z^i S_z^i)$, taken from [17]. For fixed interaction strength $J = 1$, as disorder strength h increases there is a transition from a thermalized (ETH) to a MBL phase. For finite size systems, this transition passes through a critical region that becomes smaller as the system size grows.

Appendix C

Matlab Code

Below are examples of scripts and functions used for much of the data collection in this thesis. Some faster data acquisition was done on desktop computers or a laptop, but much of the computation was done through Dartmouth's Discovery cluster. Many quantum mechanical operations such as the Schmidt decomposition and partial trace were performed using the package "QETLAB: A MATLAB Toolbox for Quantum Entanglement."

```
% Function that defines a Hamiltonian given input parameters, performs Schmidt↙
decompositions for a range of eigenvectors, then stores each Schmidt spectrum (zeta) as↙
an array in a column of the cell zetcell.

% author: Kent Ueno
% email: kentu@optonline.net

function [zetcell] = Schmidt_NMR(M,N,u,v,ximax,yimax,zimax)

tstart = tic;

% Pauli/spin matrices
z=sparse([1 0; 0 -1]); x=sparse( [ 0 1;1 0]); y=1i*sparse([0 -1;1 0]);
Sz=sparse(.5.*[1 0; 0 -1]); Sx=sparse(.5.*[ 0 1;1 0]); Sy=1i*sparse(.5.*[0 -1;1 0]);
ep=sparse([1 0; 0 0]);
em=sparse([0 0; 0 1]);
id=speye(2);p=sparse([0 1;0 0]);m=sparse([0 0; 1 0]);
dim = 2^(M+N);
dimN = 2^N;

spectrum_third = round(dim/3);          % a third of the energy spectrum size

% assign some variables to the workspace
assignin('base', 'M', M);
assignin('base', 'N', N);
assignin('base', 'dim', dim);
assignin('base', 'dimN', dimN);
assignin('base', 'u', u);
assignin('base', 'v', v);
assignin('base', 'yimax', yimax);
assignin('base', 'zimax', zimax);
assignin('base', 'zimax', zimax);

% H is the Hamiltonian that the spins evolve under
H=sparse(dim,dim);

% nearest neighbor couplings
a=sparse(diag(ones(N+M-1,1),1)+diag(ones(N+M-1,1),-1));

% build up spin chain properties
for k=1:(N+M)
    for h=k+1:(N+M)

        H=H+a(k,h)*(((u+v)/2)*mykron(speye(2^(k-1)),x,speye(2^(h-k-1)),x,speye(2^(N+M-↙
h)))+...
            ((v-u)/2)*mykron(speye(2^(k-1)),y,speye(2^(h-k-1)),y,speye(2^(N+M-h)))-...
            v*mykron(speye(2^(k-1)),z,speye(2^(h-k-1)),z,speye(2^(N+M-h))));

    end
end

% collective nuclear spin polarizations
X = sparse(dim,dim);
Y = sparse(dim,dim);
Z = sparse(dim,dim);

% build up disorder terms
for k=1:(N+M)
```

```
    xi = ximax*(-1+2.0*rand);
    X = X + xi.*mykron(speye(2^(k-1)),x,speye(2^(N+M-k)));

    yi = yimax*(-1+2.0*rand);
    Y = Y + yi.*mykron(speye(2^(k-1)),y,speye(2^(N+M-k)));

    zi = zimax*(-1+2.0*rand);
    Z = Z + zi.*mykron(speye(2^(k-1)),z,speye(2^(N+M-k)));

end

% total Hamiltonian
H = sparse(H + X + Y + Z);

% sort eigenenergies and eigenvectors in ascending order
[V,D] = eig(full(H));
[~,I] = sort(diag(D));
V = V(:,I);

clear D I;

% ground state energy
% V = V(:,1);

% middle third of eigenenergy spectrum
% V = V(:,spectrum_third:(2*spectrum_third));

% otherwise, full energy spectrum

% cell to store each array of exponential Schimdt values (zeta)
zetcell = cell(1,min(size(V)));

% Schmidt decomposition of eigenvectors
for c=1:(min(size(V)))

    S = SchmidtDecomposition(V(:,c),[2^(M),2^(N)]);

    % store each zeta array as a column of the zeta cell
    zetcell{1,c} = (-2).*log(S);
end

clear V S;

toc(tstart);
end
```

```
% For each array of Schmidt coefficients (zetas), look at the distribution of ratios of successive spacings. Loop through disorder and interaction strengths.

% author: Kent Ueno
% email: kentu@optonline.net

figure
subplot_pos = 0;                    % subplot position for plots

% loop through the dimensions of the cell containing zeta arrays
for i = 1:m
    for j = 1:n

    r_tot = [];                     % total array of ratios

    % pick out the array of zetas for an eigenvector, calculate ratios, then add to total ratio array r_tot
    for c = 1:length(cell2D{i,j})

        zet = sort(cell2D{i,j}{1,c});                       % sorted array of zetas

        % don't indlude zeta arrays that are too small
        if zet<2
        count = count + 1;
        else
        r = sparse(1,(length(zet)-2));                      % array to hold ratios of consecutive spacings for this zeta array

        % min/max ratio
        for k = 2:(length(zet)-1)
            r(k-1) = min([(zet(k+1)-zet(k)),(zet(k)-zet(k-1))])/max([(zet(k+1)-zet(k)),(zet(k)-zet(k-1))]);
        end

        % store ratios from each eigenvector into total array
        r_tot = horzcat(r_tot,r);
        end
    end

    % determine histogram bin values and bin centers
    [rhor,r2] = histcounts(r_tot,100,'Normalization','pdf');

    % center bins and normalize
    r2 = r2 + (r2(2)-r2(1))/2;
    r2(:,end) = [];
    rhor = rhor/2;

    % fit functions
    ffit = (1+r2).^(-2);                                                    %Poisson
    ffit2 = 6.*r2./((1+r2).^(4));                                           %Semi-Poisson
    gfit = ((8/27)^(-1)).*(r2+r2.^2)./((1+r2+r2.^2).^2.5);                  %GOE
    gfit2 = ((4*pi/81/sqrt(3))^(-1)).*((r2+r2.^2).^2)./((1+r2+r2.^2).^4);   %GUE

    % create subplots and plot
```

```
    subplot_pos = subplot_pos + 1;
    subplot(m,n,subplot_pos)

    hold on

    plot(r2,ffit,'LineWidth',4,'DisplayName','Poisson');
    plot(r2,ffit2,'LineWidth',4,'DisplayName','Semi-Poisson');
    plot(r2,gfit,'LineWidth',4,'DisplayName','GOE');
    plot(r2,gfit2,'LineWidth',4,'DisplayName','GUE');

    scatter(r2,rhor,36,'filled')

    % plot properties
    xlim([0,1])
    ylim([0,1])
    xlabel('r')
    ylabel('P(r)')
    set(gca,'linewidth',3)
    set(gca,'fontsize',40)
    set(gca,'TickLength',[.05,.05])
    legend('show')
    hold off

    end
end
```

```
% For each Schmidt coefficient (zeta) array, generate a density of states (DOS)↙
distribution of zetas and a distribution of normalized spacings of unfolding variable s.↙
Loop through disorder and interaction strengths.

% author: Kent Ueno
% email: kentu@optonline.net

for i = 1:m
    for j = 1:n

    z_tot = [];                     % total array of zeta density of state (DOS) values
    ds1 = [];                       % total array of spacings method 1
    ds2 = [];                       % total array of spacings method 2

    % build arrays of s and assign to scell
    for c = 1:length(cell2D{i,j})

        % array of zeta values for particular eigenstate
        zet = sort(cell2D{i,j}{1,c});                       % sorted array of zetas

        % add zeta values for each eigenvector to the array of total zeta values
        z_tot = horzcat(z_tot,zet');

        %%%%%%%%%%%%%%%%%%%%%%%%%%%%%%%%%%%%%%%%%%%%%%%%%%%%%%%%%%%%%%%%%%%%%%%
        % this section is for unfolding each eigenstate

        % use ksdensity to create smoothed density function
        [rhoy,rhox] = ksdensity(zet,zet);

        % two options for unfolding

%       % method 1: build up new variable s using unfolding procedure (from paper)
%
%       s = sparse(1,length(rhox));                 % new variable created via unfolding
%
%       % numerical integration using local averages of rhoy
%       for k = 1:length(rhox)-1
%           if k == 1
%               s(k) = .5*(rhoy(1)+rhoy(2))*(rhox(2)-rhox(1));
%           else
%               s(k) = trapz(rhox(1:k),(.5*(rhoy(2:k+1)+rhoy(1:k))));
%           end
%       end
%
%       % sort into ascending order, calculate spacings
%       s = sort(s)*length(zet); ds = diff(s);

        % method 2: build up spacings ds using unfolding procedure (Drubo thesis)
        dsa = diff(sort(zet));
        rhoy = length(zet)*rhoy;
        for k = 1:length(dsa)
            avg = 2/(rhoy(k)+rhoy(k+1));
            ds(k) = dsa(k)/avg;
        end

        % add each ds to total concatenated ds array
        ds1 = horzcat(ds1,ds);
        % ds2 = horzcat(ds2,ds);
```

```
    %%%%%%%%%%%%%%%%%%%%%%%%%%%%%%%%%%%%%%%%%%%%%%%%%%%%%%%%%%%%%%%%%%%%%%%
end

clear s rhox rhoy c k;

%%%%%%%%%%%%%%%%%%%%%%%%%%%%%%%%%%%%%%%%%%%%%%%%%%%%%%%%%%%%%%%%%%%%%%%%%%
% two options for creating the density function

% method 1: use histogram to create density function
[rhoz2,z2] = histcounts(z_tot,round(length(z_tot)/100),'Normalization','pdf');

% center bins
z2 = z2 + (z2(2)-z2(1))/2;
z2(end) = [];

% method 2: use ksdensity to create density function
[rhoy2,rhox2] = ksdensity(z_tot,'NumPoints',length(z_tot)/100);

% compare histogram and ksdensity DOS functions
figure
hold on
scatter(z2,rhoz2);
scatter(rhox2,rhoy2);
% xlim([0,25]);
hold off

%%%%%%%%%%%%%%%%%%%%%%%%%%%%%%%%%%%%%%%%%%%%%%%%%%%%%%%%%%%%%%%%%%%%%%%%%%


% histogram spacing values with DOS normalization
[P_ds1,ds3] = histcounts(ds1,300,'Normalization','pdf','BinLimits',[0,5]);

% center bins for P_ds1
ds3 = ds3 + (ds3(2)-ds3(1))/2;
ds3(end) = [];

figure
% subplot_pos = subplot_pos + 1;
% subplot(m,n,subplot_pos)

hold on

% plot RMT distributions
plot(ds3,distribs(1,0,ds3),'LineWidth',2,'DisplayName','Poisson');
plot(ds3,distribs(1,1,ds3),'LineWidth',2,'DisplayName','Semi-Poisson');
plot(ds3,distribs(0,1,ds3),'LineWidth',2,'DisplayName','GOE');
plot(ds3,distribs(0,2,ds3),'LineWidth',2,'DisplayName','GUE');

% plot total spacings distribution
scatter(ds3,P_ds1,25,'filled');

% plot properties
xlim([0,5])
ylim([0,1])
xlabel('s')
ylabel('P(s)')
set(gca,'linewidth',1.5)
```

```
    set(gca,'fontsize',28)
    legend('show')
    hold off

    end
end
```

```
% Create a color plot showing the strength of fit to the GOE distribution.

% author: Kent Ueno
% email: kentu@optonline.net

% matrix to store fit values
fitmat = sparse(m,n);

% loop through parameter space
for i = 1:m
    for j = 1:n

    r_tot = [];                     % total array of ratios

    % pick out the array of zets for an eigenvector, calculate ratios, then add to total↙
ratio array r_tot
    for c = 1:length(cell2D{i,j})

        zet = sort(cell2D{i,j}{1,c});                       % sorted array of zetas

        if length(zet) < 3
        else
        r = sparse(1,(length(zet)-2));                      % ratios of consecutive↙
spacings

        % min/max ratio
        for k = 2:(length(zet)-1)
            r(k-1) = min([(zet(k+1)-zet(k)),(zet(k)-zet(k-1))])/max([(zet(k+1)-zet(k)),↙
(zet(k)-zet(k-1))]);
        end

        r(isnan(r(:))) = [];

        % store ratios from each eigenvector into total array
        r_tot = horzcat(r_tot,r);
        end
    end

    % clear c k;

    % determine histogram bin values and bin centers
    [rhor,r2] = histcounts(r_tot,300,'Normalization','pdf','BinLimits',[0,1]);
    r2 = r2 + (r2(2)-r2(1))/2;
    r2(:,end) = [];

    rhor = rhor/2;

    % fit functions
    ffit = (1+r2).^(-2);                                                    %↙
Poisson
    ffit2 = 6.*r2./((1+r2).^(4));                                           %↙
Semi-Poisson
    gfit = ((8/27)^(-1)).*(r2+r2.^2)./((1+r2+r2.^2).^2.5);                  %↙
GOE
    gfit2 = ((4*pi/81/sqrt(3))^(-1)).*((r2+r2.^2).^2)./((1+r2+r2.^2).^4);   %↙
GUE

    % fit to linear combination of SP and GOE
```

```
    myfittype_lin = fittype('b*(6.*r2./((1+r2).^(4)))+c*(((8/27)^(-1)).*(r2+r2.^2)./↙
((1+r2+r2.^2).^2.5))','dependent',{'rho_r'},'independent',{'r2'},'coefficients',↙
{'b','c'});
    myfit_lin = fit(r2',rhor',myfittype_lin,'StartPoint',[0,0],'Lower',[0,0],'Upper',↙
[1.5,1.5]);

    % get coefficients
    coeff = coeffvalues(myfit_lin);

    % save normmalized fit to GOE
    fitmat(i,j) = coeff(2)/(sqrt(coeff(1)+coeff(2)));

    end
end

% plot properties
colormap(hot)
imagesc(fitmat);
colorbar
caxis([0,1])
title('Fit strength to GOE: 14 spins, 8-6 partition')
xlabel('v')
ylabel('g')
set(gca,'XTickLabel',0:.1:1);
set(gca,'YTickLabel',1:9);
set(gca,'linewidth',1.5)
set(gca,'fontsize',28)
```

```
% Function that defines and evolves a random product state given certain input parameters↙
to the Hamiltonian.

% author: Kent Ueno
% email: kentu@optonline.net

function [rhoLcell] = ESS_NMR(M,N,u,v,g,tfin,init_reals,H_reals)

tstart = tic;

% Pauli matrices
z=sparse([1 0; 0 -1]);x=sparse( [ 0 1;1 0]); y=1i*sparse([0 -1;1 0]);
ep=sparse([1 0; 0 0]);
em=sparse([0 0; 0 1]);
id=speye(2);p=sparse([0 1;0 0]);m=sparse([0 0; 1 0]);
dim = 2^(M+N);

assignin('base', 'M', M);
assignin('base', 'N', N);
assignin('base', 'dim', dim);
assignin('base', 'dimN', 2^N);
assignin('base', 'g', g);
assignin('base', 'u', u);
assignin('base', 'v', v);
assignin('base', 'tfin', tfin);
assignin('base', 'init_reals', init_reals);
assignin('base', 'H_reals', H_reals);

% nearest neighbor couplings
a=diag(ones(N+M-1,1),1)+diag(ones(N+M-1,1),-1);

% random Psi
up = [1,0];
down = [0,1];

% H is the Hamiltonian that the spins evolve under
H=sparse(dim,dim);

% build up Hamiltonian
for k=1:(N+M),

    for h=k+1:(N+M)

        H=H+a(k,h)*(((u+v)/2)*mykron(speye(2^(k-1)),x,speye(2^(h-k-1)),x,speye(2^(N+M-↙
h)))+...
            ((v-u)/2)*mykron(speye(2^(k-1)),y,speye(2^(h-k-1)),y,speye(2^(N+M-h)))-...
            v*mykron(speye(2^(k-1)),z,speye(2^(h-k-1)),z,speye(2^(N+M-h))));

    end

end

% cell to store rhoL matricies
rhoLcell = cell(init_reals,H_reals);

% build up initial state and time evolve; iterate over number of realizations
for r=1:init_reals,
realtime = tic;
```

```
    Psi_rand = 1;

    for j=1:(M+N),
        angles = 2*pi.*rand(3,1);
        theta = angles(1);
        phi1 = angles(2);
        phi2 = angles (3);

        new_rand = exp(1i*phi1)*cos(theta).*up+exp(1i*phi2)*sin(theta).*down;
        Psi_rand = mykron(Psi_rand,new_rand);
    end

    % define random intial state
    rho = Psi_rand'*Psi_rand;

    for i=1:H_reals,

        % collective nuclear spin polarizations
        Z = sparse(dim,dim);
        X = sparse(dim,dim);

        % build up disorder terms
        for k=1:(N+M),

            gzi = g*(-1+2*rand);
            Z = Z + gzi*mykron(speye(2^(k-1)),z,speye(2^(N+M-k)));

            gxi = g*(-1+2*rand);
            X = X + gxi*mykron(speye(2^(k-1)),x,speye(2^(N+M-k)));

        end

        % total Hamiltonian
        H = H + X + Z;

        % define Unitary operator for time step
        U=sparse(expm(-1i*Htot*tfin));

        % evolve quantum state
        Psi_t=U*Psi_rand';

        % density matrix
        rho = Psi_t*Psi_t';

        % store partial trace onto left
        rhoLcell{r,i} = PartialTrace(rho,1,[2^M,2^N]);
    end
toc(realtime);
end

clear new_rand angles theta phi1 phi2;
toc(tstart);
```

```
% For each ESS eigenvalue array, compute ratios of adjacent spacings. Loop through↙
parameter space.

% author: Kent Ueno
% email: kentu@optonline.net

figure
subplot_pos = 0;

% fit function coefficients
C2 = gamma(3)/gamma(2);
C1 = (C2^2)/gamma(2);

% fit functions
xfit = 0:.001:10;
ffit = (1+xfit).^(-2);                                                          %↙
Poisson
ffit2 = C1*xfit.*exp(-C2*xfit);                                                 %↙
Semi-Poisson
gfit = ((8/27)^(-1)).*(xfit+xfit.^2)./((1+xfit+xfit.^2).^2.5);                  % GOE
gfit2 = ((4*pi/81/sqrt(3))^(-1)).*((xfit+xfit.^2).^2)./((1+xfit+xfit.^2).^4);   % GUE

% loop through parameter space
for par_i = 1:n
    for par_j = 1:m

    % eigenvalue ratios
    eg_ri = zeros(1,dimN-2);       % array to store ratios of consecutive spacings for↙
each iteration
    eg_ritot = [];                 % total array of eigenvalue ratios

    for i=1:size(cell2D{par_i,par_j},1)
        for j=1:size(cell2D{par_i,par_j},2)

            % Array of sorted eigenvalues in descending order
            eg = flip(sort(real(eig(cell2D{par_i,par_j}{i,j}))));

            % compute ratios
            for k = 2:(dimN-1)
                eg_ri(k-1) = (eg(k-1)-eg(k))/(eg(k)-eg(k+1));
            end

            % store in total ratio array
            eg_ritot = horzcat(eg_ritot, eg_ri);

        end
    end

    % histogram properties
    [h_eg,edges] = histcounts(eg_ritot,300,'Normalization','pdf','BinLimits',[.01,10]);
    x_eg = edges + (edges(2)-edges(1))/2;
    x_eg(:,end) = [];

%   subplot_pos = subplot_pos + 1;
%   subplot(m,n,subplot_pos)

    % plot data
    hold on
```

```
    set(gca,'linewidth',1.5)

    scatter(x_eg,h_eg,36,'filled')

    plot(xfit,ffit,'Color','r','LineWidth',2,'DisplayName','Poisson')↙
% Poisson
    plot(xfit,gfit,'Color','g','LineWidth',2,'DisplayName','GOE')↙
% GOE
    plot(xfit,gfit2,'Color','k','LineWidth',4,'DisplayName','GUE')↙
% GUE

    % plot properties
    xlim([.1,10])
    ylim([.001,1])
    set(gca,'YScale','log')
    set(gca,'XScale','log')
    title(['$\Delta = $ ' num2str(delt(par_j)) ', $z_i \in [-$' num2str(hmax(par_j)) '$,$↙
' num2str(hmax(par_j)) '$]$'],'Interpreter','latex')
    set(gca, 'FontSize',40)
    set(gca,'LineWidth',3)
    set(gca,'TickLength',[.05,.05])
    xlabel('r')

    if subplot_pos==1
    ylabel('P(r)')
    end

    legend('show')
    hold off

    end
end
```

```
function PO=mykron(varargin)
%function PO=mykron(varargin)
% This little function allows you to pass all of
% the product operators in at once and it goes through
% and makes the right answer.  It is equivalent to
% kron(kron(kron(x,x),x),x)....
% written April 29th 2000, -Evan Fortunato

if length(varargin) < 1,
    error('Please enter atleast 1 Product Operator!');
elseif length(varargin) == 1,
    PO = varargin{1};
else,
    PO = varargin{1};
    for j=2:length(varargin),
        PO=kron(PO, varargin{j});
    end;
end;
```

```
% function to compute distributions when given input values

% author: Kent Ueno
% email: kentu@optonline.net

function distrib = distribs(g,a,x)

    % function coefficients
    C2 = (gamma((2+a)/(2-g))/gamma((1+a)/(2-g)))^(2-g);
    C1 = ((2-g)*(C2^((1+a)/(2-g))))/gamma((1+a)/(2-g));

    distrib = C1*(x.^a).*exp(-C2*(x.^(2-g)));

    %clear C1 C2;
```

Bibliography

[1] Alisa Bokulich and Gregg Jaeger. *Philosophy of Quantum Information and Entanglement*. Cambridge University Press, New York, NY, USA, 1st edition, 2010.

[2] Krishan Canzius. *Entanglement Metrics for Quantum Spin Chains*. Undergraduate honors thesis, Department of Physics and Astronomy, Dartmouth College, 6 2018.

[3] Rahul Nandkishore and David A. Huse. Many-body localization and thermalization in quantum statistical mechanics. *Annual Review of Condensed Matter Physics*, 6(1):15–38, 2015.

[4] David A. Huse, Rahul Nandkishore, and Vadim Oganesyan. Phenomenology of fully many-body-localized systems. *Phys. Rev. B*, 90:174202, Nov 2014.

[5] P. W. Anderson. Absence of diffusion in certain random lattices. *Phys. Rev.*, 109:1492–1505, Mar 1958.

[6] Mehran Kardar. *Statistical Physics of Fields*. Cambridge University Press, 2007.

[7] Scott D. Geraedts, Rahul Nandkishore, and Nicolas Regnault. Many-body localization and thermalization: Insights from the entanglement spectrum. *Phys. Rev. B*, 93:174202, May 2016.

[8] Vadim Oganesyan and David A. Huse. Localization of interacting fermions at high temperature. *Phys. Rev. B*, 75:155111, Apr 2007.

[9] Zhi-Cheng Yang, Alioscia Hamma, Salvatore M. Giampaolo, Eduardo R. Mucciolo, and Claudio Chamon. Entanglement complexity in quantum many-body dynamics, thermalization and localization. 2017.

[10] C.P. Slichter. *Principles of Magnetic Resonance*. Springer Series in Solid-State Sciences. Springer-Verlag Berlin Heidelberg New York, 1978.

[11] Ken Xuan Wei, Chandrasekhar Ramanathan, and Paola Cappellaro. Exploring localization in nuclear spin chains. 2016.

[12] P. Jordan and E. Wigner. Über das paulische äquivalenzverbot. *Zeitschrift für Physik"*, 47(9):631–651, Sep 1928.

[13] Rajibul Islam, Ruichao Ma, Philipp M. Preiss, M. Eric Tai, Alexander Lukin, Matthew Rispoli, and Markus Greiner.

[14] Y. Y. Atas, E. Bogomolny, O. Giraud, and G. Roux. Distribution of the

ratio of consecutive level spacings in random matrix ensembles. *Phys. Rev. Lett.*, 110:084101, Feb 2013.

[15] Maksym Serbyn and Joel E. Moore. Spectral statistics across the many-body localization transition. *Phys. Rev. B*, 93:041424, Jan 2016.

[16] Nicolas Regnault and Rahul Nandkishore. Floquet thermalization: Symmetries and random matrix ensembles. *Phys. Rev. B*, 93:104203, Mar 2016.

[17] S D Geraedts, N Regnault, and R M Nandkishore. Characterizing the many-body localization transition using the entanglement spectrum. *New Journal of Physics*, 19(11):113021, 2017.

[18] Ashraf A. Abul-Magd and Adel Y. Abul-Magd. Unfolding of the spectrum for chaotic and mixed systems. *Physica A: Statistical Mechanics and its Applications*, 396:185 – 194, 2014.

[19] Drubo Jyoti. *Dipolarly-Coupled Chaotic Quantum Spin Systems.* Undergraduate honors thesis, Department of Physics and Astronomy, Dartmouth College, 6 2011.

[20] Dmitry A. Abanin, Ehud Altman, Immanuel Bloch, and Maksym Serbyn. Ergodicity, entanglement and many-body localization. 04 2018.

[21] Fritz Haake. *Quantum Signatures of Chaos.* Springer-Verlag, Berlin, Heidelberg, 2006.

[22] R. Vasseur, S. A. Parameswaran, and J. E. Moore. Quantum revivals and many-body localization. *Phys. Rev. B*, 91:140202, Apr 2015.